Multidimensional Diffusive Shock Acceleration in the Winds from Massive Stars

A DISSERTATION
SUBMITTED TO THE FACULTY OF THE GRADUATE SCHOOL
OF THE UNIVERSITY OF MINNESOTA
BY

Paul Pretzer Edmon

IN PARTIAL FULFILLMENT OF THE REQUIREMENTS
FOR THE DEGREE OF
Doctor Of Philosophy

Thomas W. Jones, Advisor

July, 2010

Acknowledgements

First and foremost, given the mentally arduous and emotionally taxing nature of this work I first would like to thank God for sustaining me through it all. It is only by divine providence that I have made it this far, in spite of my own failings. Thus it is appropriate that I thank Him who created it all and continues to sustain it.

Wow, I'm sure that any transition I could provide from that first paragraph would be sufficiently awkward so I will just move on. I would like to thank my advisor Tom Jones for his guidance through this entire process. Tom's approach to astronomy, and science in general, deserves to be lauded. He has a knack for reducing even the most complex problems down to tractable back of the envelope calculations. His dedication to science and his students is amazing. For even when he had impending deadlines or was exceedingly busy with being the MSI Interim Director, he would always make time to look at a new simulation we had been working on or help us to work through an idea we had. I truly appreciate everything I learned from him, and I can only hope that it has made me into a scientist with even a tenth of his skill. I also hope he can now take at least a little break to go play with Cosmo, or take a trip to Brazil, after managing graduate students, teaching classes, reviewing articles and proposals, and running the MSI.

Another person I owe a great debt to in the completion of this thesis is Peter Mendygral. He has been an outstanding office mate and friend for the past 4 years. I can safely say that this entire project would have been dead in the water without Pete's help. Pete's coding prowess combined with his insatiable desire to learn brought forth WOMBAT, which has become the pride of our group. In addition, being able to bounce theories and other crazy ideas off of Pete has been invaluable. Hopefully, I have been as helpful to him as he has been to me, and that we will be able to continue to collaborate

on future projects. I wish him the best in his future scientific pursuits and success with his new family.

The staff and facilities at the MSI have been invaluable in the completion of this work. Our computers were always kept in fantastic condition, we always had access to the latest and greatest programs and technologies, and there was an abundance of excellent free food. The technical support provided by David Porter and Mike Knox helped me many times through out this process. David was always a willing ear to bounce ideas off of or to query for instruction in the fine arts of parallelization and data analysis. Mike, on the other hand, provided our group with access and support for Paul Woodward's cluster for which we are immensely grateful for. Paul Woodward should also be thanked for allowing us to use the resources that he has built up here at the University. They have all been extremely useful in my research.

My collaborators have also been great help to my research. Adam Frank and his group at University of Rochester have put great pains into their AstroBEAR code, and I am grateful for the opportunity to contribute to their work. Hyesung Kang and Dongsu Ryu were fantastic hosts when I was in Korea, and Hyesung has been a valued collaborator. Her patience has been astounding. Hopefully we will finally get the SNR paper published after this three year ordeal.

I would be remiss if I also did not thank the funding agencies who chose to fund this research. This work was funded on both NASA and NSF grants, without which none of this work would have been possible. Their continued support of science and technology are the crucial for many endeavors in these fields.

The faculty, staff and graduate students of the Astronomy Department have been a great support to me during my time here. The instruction I received from the faculty has been top class. Specifically I would like to thank Liliya Williams, Terry Jones and Bob Lysak for being on both my preliminary oral exam and final exam committees. All of their classes have been incredibly helpful in my development as a scientist. Terry Thibeault, Corinne Komor and the plethora of student secretaries have helped to keep me paid and on track for my eventual departure. The graduate students have provided a fantastic environment to work in, as well as providing needed distraction, entertainment and support.

My predecessor Sean O'Neill helped to familiarize me with the MSI and the interesting people that resided there. Plus he was the one who first invited me to join HARG. HARG allowed me to continue to study history, both ancient and modern, and to do so in a light I had not thought about before, that of History of Science. Aimee, Sean, Maggie, Tom, Andrew, Nick, Adrian, Chelsea, Andrea, Sara, Simon, Amy and I have had great discussions and debates about various interesting parts of history. I hope that the group will survive the departure of the last two of its original members but if not it has been a fantastic 5 years.

Andrew Helton has been a good friend who was always willing to discuss movies at the drop of a hat. Steve Warren has provided many a good reason to go out and get breakfast or sit outside and discuss research. Jennifer Delgado helped in many ways to make WOMBAT into the code it is today.

Dain, Martha, Pete and Jennifer have all done a fantastic job coordinating our outreach efforts. Doing outreach, both during the school year and for UitP, has been a joy for me. The opportunity to go out and talk about a topic that so many people love and are extremely interested in is one of the great points of being in this department. The commitment to outreach has been unparalleled and I am proud to have been a part of it. I will greatly miss it when I am gone.

My family and friends have also provided much support and encouragement through this entire process. My parents especially have been very supportive. Their love and care for me through out my life has been a real blessing. Their willingness to financially support three children through undergraduate education has been an inspiration and critical to my success here. The additional inspiration provided by my father in regards to obtaining a doctorate has been invaluable. For after all it was his status as doctor that helped motivate me to obtain the same status. The support by both my mother and father for my passion for space has been outstanding.

My brother and sister have provided me with much needed laughs and support as well. While they may have harassed me much of time, their continued belief in me and my abilities has been very important. Also the time that Tim and I spent playing games together during my time here has been a blast. I hope we continue to play well in to the future.

My friends from my days at University of Washington have continued to provide

many worthy distractions and much support. Many an epic fight or meal has fallen to our might. The imagination and drive displayed by them has inspired me to push forward with my own dreams and has kept my imagination vibrant.

My friends here in Minneapolis have also been very supportive. KC and Matt have been great friends and worthy philosophers. The discussions we held while watching Twins games were both edifying and hilarious. I wish them well in their future pursuits.

My friends and church family at University Lutheran Chapel have been a foundation of spiritual guidance and theological training. I am proud to have served as their congregational president for two years. Their commitment to the purity of the Gospel and the historic liturgy is the model for all congregations. The theological depth of their teaching has been a phenomenal source of my growth as a Lutheran. Pastor Kind has been a steady shepherd and good friend through all of this. Him and his family have shown me the utmost kindness and have been a joy to be with.

All the families at ULC have all been incredibly supportive of my studies. Gary and Monica Elsesser, in particular, have always been willing to have me at their home and Gary is always willing discuss any math problem that comes to mind. My fellow students have also been great companions on this journey. The Linke sisters have been a blast to hang out with. Matt Rothchild's exploits are to this day astounding to me. Matttias Gassman has an encyclopedic knowledge of ancient literature that I can only dream about. The Beach's have supported me since the moment I arrived. I wish them all well in the future. While I may move on to other congregations, know that the instruction I received at ULC will be carried with me into eternity.

Finally, I would like to thank those who have produced the great and varied instruments which have provided mental relief through the years. TV, games, books, movies, music, and webcomics have been much needed distractions from my mental fervor in completing this project. In particular, I would like to thank Arena.Net who made Guild Wars for providing an outstanding game which captivated me and my brother for 3 years. I look forward to GW2 and more epicness. I would also like to thank those companies who translate, import and produce anime. Anime has been a continual source of imaginative and inspiring stories for me. The sheer creativity displayed in some of these works boggles my mind. The libraries at the U of M have been a great resource in my own hobby of reading mythology, I will be sad to lose access to them. Penny

Arcade and its epic spin off the Epic Legends of the Heirarchs have also been a great lunch time break.

While I could go on for pages more about those who have helped me to reach my degree I will stop here for the sake of brevity. Know that I truly and deeply appreciate all those who have contributed to this work or my continued sanity even if I did not mention you. Again thank you all and enjoy reading this thesis!

Dedication

To all those who have gone before me in this most ancient and esteemed field of study.

Abstract

Nonthermal radio emission has been seen in the winds around a quarter of all O-stars. The emission is attributed to shock accelerated cosmic rays. The shocks thought to be causing the acceleration are either wind-embedded shocks due to radiative line driving instabilities in the stellar wind, or shocks due to the colliding winds in a binary system. Very few numerical Diffusive Shock Acceleration (DSA) simulations exist for these systems due to the complicated, multidimensional nature of the winds. We present the first 2-D magnetohydrodynamic DSA (MHD-DSA) simulations of massive stellar winds using the Multidimensional Adaptive Subcycling Tridiagonal solver (MAST), which has been incorporated into the WOMBAT (sWift Objects for Mhd BAsed on Tvd) code to solve diffusive shock acceleration for cosmic rays. Shock modification due to cosmic ray pressure is shown to be important in describing the shock dynamics of the colliding wind binary scenario. With 10^{-4} of the gas particles passing through the shocks being injected as cosmic rays, about 15% of the wind ram pressure is converted into cosmic ray pressure. In the wind-embedded shock scenario, the isothermal conditions in the wind, due to radiative heating and cooling, precluded inclusion of cosmic ray feedback. Future 1-D simulations of cosmic ray modified radiative shocks are suggested, as the combined effects of radiative line cooling and cosmic ray feedback dramatically change the shock dynamics from adiabatic analogues. Both cases show efficient cosmic ray acceleration. In the case of the wind-embedded shocks, the isothermal nature of the wind creates shocks capable of accelerating electrons up to 100 MeV and protons up to 1 GeV with a spectral slope of 4. The colliding wind binary scenario produces very strong shocks which are capable of accelerating electrons up 1 GeV and protons up to 1 TeV with a spectral slope of 4. While full radiation models will be performed in the future, preliminary estimates indicate that the radio emission from the wind-embedded

shock scenario may be extinguished due to free-free absorption. This would exclude the wind-embedded shock scenario from being able to explain the observed radio emission.

Contents

List of Tables

List of Figures

Chapter 1

Introduction

1.1 O-star Winds

O-stars are the most massive stars in the universe. The masses of these stars typically range from $20 - 100$ $M_\odot$. Along with their high mass they also have very high surface temperatures of $30,000 - 50,000$ Kelvin. These high temperatures make O-stars powerful blackbody emitters with spectral peaks in the near ultraviolet and luminosities in the range of $10^5 - 10^8$ $L_\odot$.

The extreme conditions at the surface of these stars lead to strong radiatively driven stellar winds. The radiative driving is caused by the mighty radiation field emitted by the star. As the photons escape from the surface of the star they scatter off atomic transition lines in the outer atmosphere of the star. This transfers enough momentum to overcome the gravity of the star and accelerate the material. The densities in the wind create a sufficiently high opacities such that all the emission at the line frequencies is scattered. That being the case the scattered radiation is unavailable for acceleration further out in the wind. However, as the material accelerates the transition lines in the wind are Doppler shifted. This allows the material to interact with higher energy photons which were not scattered by the inner wind. Thus the wind continues to accelerate.

Eventually the material moves far enough from the star that it no longer gains significant momentum. At this point the flow reaches its terminal velocity, typically around $1000 - 3000$ km/s. Large amounts of material is lost from the star in the

process, around $10^{-6} - 10^{-4}$ $M_{\odot}$ per year (see Lamers & Cassinelli (1999) for a full discussion).

The severe winds interact with the surrounding interstellar medium (ISM). Large wind blown bubbles are created which are parsecs in scale (Cappa et al. 2003). It is in this environment that the O-star will eventually die in a catastrophic supernova (Dwarkadas 2005). The resulting shockwave will propagate into the bubble. The interaction with the bubble can dramatically effect the evolution of the resulting remnant.

It is also the case that O-stars are commonly found in groups and clusters near where they are born. The collective winds from these systems can give rise to bubbles that can occupy tens to hundreds of parsecs (Chu 2008). The shocks driven from these winds can trigger new star formation in surrounding molecular clouds (Lee & Chen 2009). Supernovae from the cluster of O-stars can also blow large holes in the gas of the galaxy (Mac Low et al. 1989).

The large scale impacts of the winds from O-stars make it imperative to understand the dynamics of these winds. While the acceleration mechanism for O-star winds is well understood, there is still much about the character of these winds to be investigated. Among these puzzles are questions about the clumpiness of the wind, the role of the magnetic field, and the morphology of the outflows (Fullerton et al. 2006; De Becker 2007; Cranmer & Owocki 1996).

1.1.1 Nonthermal Radio Emission

One of the big observational puzzles about O-star winds comes from radio observations. The majority of radio emitting O-stars can be explained as thermal bremsstrahlung emission in the stellar wind (Wright & Barlow 1975; Panagia & Felli 1975). However, about a quarter of radio emitting O-stars cannot be explained by this model (Bieging et al. 1989). The spectral index of these winds is found to deviate significantly from that expected for thermal bremsstrahlung emission in these systems (De Becker 2007). The brightness temperature of the emission is also found to be too high to be explained via thermal bremsstrahlung.

This nonthermal emission is thought to be due to radio synchrotron (White 1985). Synchrotron emission implies that relativistic cosmic ray (CR) electrons are being accelerated in the wind. The acceleration mechanism responsible for the electrons is theorized

to be shocks in the wind.

1.2 Diffusive Shock Acceleration

The leading theory for CR acceleration at astrophysical shocks is Diffusive Shock Acceleration (DSA) (e.g., Malkov & O'C Drury (2001) and references therein). DSA accelerates particles through a first order Fermi process. Initially CRs are injected into this process from the high energy tail of the thermal particle distribution. The injected particles must have sufficient energy to cross the shock and propagate upstream. As they do, they encounter Alfvén waves generated by the shock. The particles scatter off these Alfvén waves and eventually are reflected back towards the shock. Since the flow appears to be approaching in the particle frame when it is scattered, the particle gains energy from the flow.

When the particle crosses the shock back in to the postshock region it encounters more Alfvén waves. The particle will scatter and head back upstream. In the particle's frame the postshock flow appeared to be approaching, so the particle gains more energy from the flow. After the particle crosses back upstream it will begin the process all over again.

This scattering is a diffusive process which occurs over a characteristic length of the particle's gyroradius. As the particle gains energy it will travel further and further from the shock before it is reflected. Eventually the particle will leave the system. Particle escape is determined either by the particle being randomly scattered out of the system, or by the particle gyroradius being larger than the scale of the system.

DSA has been confirmed in-situ via heliospheric measurements and through comparisons of models to observations for various astrophysical objects (e.g., Malkov & O'C Drury (2001); Ellison et al. (1990, 1993); Berezhko et al. (1994); Drury & Völk (1981); Drury (1983); Kang et al. (2002)). It has two main modeling regimes, test particle and nonlinear. In test particle DSA, the CRs do not contain a significant amount of energy density, as compared to the gas (e.g., Malkov & O'C Drury (2001); Drury (1983); Marcowith & Kirk (1999)). Hence the CRs do not effect the flow dynamics. In these cases, DSA produces a powerlaw CR spectrum, $f(p) \propto p^{-q}$. The powerlaw slope, q, is dependent on the shock compression ratio, χ, by the relation $q = 3\chi/(\chi - 1)$

(Blandford & Eichler 1987). This is due to the DSA process being sensitive to the velocity convergence at the shock. The shock velocity convergence determines the incoming flow velocity that the particles perceive when they cross the shock. The larger the flow convergence at the shock the greater the perceived flow speed by the CR. Thus for a strong shock with a compression ratio of 4 the slope is also 4.

In nonlinear DSA, the CRs feedback on the dynamics (e.g., Malkov & O'C Drury (2001)). CR feedback comes via an additional pressure on the gas attributed to the CRs due to their large energy density. CR feedback can modify the shock, changing its Mach number and morphology.

Shocks that are strongly CR modified can have much larger compression ratios than regular adiabatic shocks. This is due to the CR pressure creating a shock precursor. The precursor originates from CRs diffusing ahead of the shock and interacting with the gas. This interaction compresses and heats the gas before it encounters the shock, essentially warning the gas about the impending shock. The preheating of the shock also reduces the shock Mach number due to the increase in the preshock sound speed. In the normal nomenclature of CR modified shocks the entire region of both the normal gas shock and the CR precursor are termed as the "shock". The normal gas shock where the discontinuity in density, velocity and pressure occurs is termed the "subshock".

All of these changes to the shock also change the CR spectrum such that it is no longer a single powerlaw but rather takes on a curved spectrum (Kang et al. 2009). Particles at low energy only see the subshock, which has been weakened by the CR precursor, as their diffusion lengths are small. At higher energy the particle diffuse further and start seeing the CR precursor as well. The additional compression from the precursor makes the shock compression look strong. Thus the spectrum is steep at low energy as it only detects the subshock compression. The spectrum becomes flatter at high energy where the shock compression is higher due to the CR precursor.

1.3 Shock Models

While DSA can explain the acceleration it does not explain the origin of the shocks. Two scenarios have been proposed to generate the shocks in the wind. The current favored model is that of a colliding wind binary (e.g., De Becker (2007) and references

therein). In this scenario two O-stars are in close enough proximity that their winds interact strongly. When this occurs very strong shocks are created which bound the wind interaction region.

The other scenario utilizes shocks embedded in the wind. The shocks originate from instabilities in the radiative line driving (White 1985; Chen 1992; Chen & White 1994). The instability itself is set off by a high velocity perturbation in the wind, which is radially interior to a slower perturbation. The high velocity perturbation Doppler shifts the lines in the perturbation, such that they scatter photons that would have normally traveled further into the undisturbed wind. This scattering drives the feature to accelerate. The lines in the slow component are Doppler shifted, such that no photons interact with this component as the photons are scattered by interior wind, which is at the same velocity. This causes the perturbation to grow as the high velocity component is accelerated, and the low velocity component stagnates. This feature will eventually steepen into a shockwave (see Lamers & Cassinelli (1999) for a full discussion).

These instabilities are randomly generated and could explain the observed clumpiness of O-star winds (Owocki 2009). While this scenario is commonly used to explain nonthermal emission in the case of a solitary O-star, these instabilities are also expected to occur in binary systems. However, in binaries any emission from the instabilities is expected to be dwarfed by the colliding wind region with its large high velocity shocks.

With an eye towards further understanding the origins of the nonthermal emission several groups have looked from an observational perspective (e.g., van Loo et al. (2006); Pittard (2009); De Becker et al. (2009); Benaglia (2010); Blomme (2010)). In many cases nonthermal radio emitting O-stars are discovered to be binaries lending credence to the colliding wind binary theory (van Loo et al. 2006). In fact, this relation of nonthermal activity to binarity has already been firmly established for Wolf-Rayet (WR) stars (Dougherty & Williams 2000). However, in the case of O-stars there are still a few stars which no binary companion has been detected (van Loo et al. 2006).

Observations in the X-ray indicate that some of these stars also have nonthermal components in that band (e.g., De Becker et al. (2004)). Radiation at these energies results from either inverse Compton (IC) or synchrotron from CR electrons in the wind. It is expected, however, that in most cases the X-ray domain will be dominated by thermal X-rays at the shock (De Becker 2007). There are also some indications that

colliding wind binaries emit in TeV γ-rays. In the case of Westerlund 2 a colliding wind WR binary, WR 20a, lies close to the emission centroid (Aharonian et al. 2007). Emission in this band would require TeV energy particles interacting via IC, if electrons, or proton-proton collisions producing neutral pions.

Theoretically it is easy to explain the emission as originating from a colliding wind binary (De Becker 2007). That scenario obviously produces two strong shocks that bound the wind interaction region, which are capable of accelerating particles. Several groups have either run hydrodynamical simulations of the wind collision region, or provided analytic solutions to the CR distribution based on the expected flow dynamics with the intent of recreating the emissions (e.g., Pittard et al. (2006); Pittard & Dougherty (2006); Reimer et al. (2006)). These methods have thus far relied on models of CR acceleration based on test particle DSA.

The wind instability scenario is not as cut and dry. It is unclear whether shocks generated by the instability described above would be prolific enough to produce the radiation. Recently van Loo et al. (2006) constructed a simple model using test particle solutions of the CR spectrum at wind-embedded shocks to try to replicate the radio spectrum. They found that in order to mimic the radio spectrum one spatially large, strong shock or multiple spatially small, strong shocks were required. van Loo et al. (2006) indicated that it was unlikely that the wind instability scenario could generate either of these cases. While the wind instability would generate multiple shocks it is expected that the shocks will get weaker as they propagate out from the star reducing their ability to accelerate particles (Runacres & Owocki 2005). Therefore, the favored scenario is that of a colliding wind binary.

1.4 Numerical Simulation of DSA

Full CR acceleration models of these systems including CR feedback on the fluid dynamics have not been executed. They have been computationally prohibitive owing to the multidimensional nature of these systems. These simulations are important because if CR feedback is strong enough it can dramatically change the shock dynamics and CR spectrum. Also, particles can be accelerated at both shocks in the colliding

wind, or at multiple shocks embedded in the wind. This requires that the CRs diffuse the distance between shocks without losing significant amounts of energy. All of these effects can dramatically change the expected emission spectrum. Thus to gain a fuller physical understanding of the CR dynamics in these systems, and to fully rule out the wind-embedded scenario, full CR modeling needs to be done (Pittard & Dougherty 2006).

Nonlinear features of DSA make it important to numerically model the time dependent effects. One method for solving the time dependent effects is to treat DSA as a continuum process and couple the DSA dynamics to the ambient fluid dynamics. These type of solvers are called kinetic solvers (see Chapter 2). Computational convergence constraints require that the simulation resolve the characteristic CR diffusion length (Jones & Kang 2005). As noted above the diffusion length is expected to be proportional to the gyroradius of the particle in astrophysical settings (Blandford & Eichler 1987). With relevant CR momenta typically spanning several orders of magnitude, the above constraint requires a large spatial grid with fine spatial resolution. Several techniques have been implemented to reduce the computational cost associated with the wide range of relevant scales. These include Berezhko et al. (1994) method for normalizing the spatial variable by the diffusion length, Kang et al. (2001) implementation of adaptive mesh refinement (AMR) to DSA, and Jones & Kang (2005) Coarse-Grained Momentum finite Volume (CGMV) method to reduce the computational expense of DSA.

Still even with these techniques kinetic solvers have been limited to systems which could be reduced by symmetry to a single spatial dimension, and typically only a single shock. This restriction excludes a wide array of astrophysical situations from full DSA modeling. Among those situations excluded are colliding wind binaries, stellar winds with internal shocks, supernova remnants in complex environments, open star clusters, and jets which are all inherently multidimensional. While approximate 1-D models could be constructed, the missing complexity and lack of multidimensionality severely inhibits the usefulness of the exercise for our physical understanding.

1.5 Thesis Outline

Recent improvements in the efficiency of kinetic DSA solvers, namely CGMV which is discussed in Chapter 2, have made it practical to begin developing multidimensional solvers. We present in Chapter 2 of this thesis, to our knowledge, the first such solver called MAST (Multidimensional Adaptive Subcycling Tridiagonal solver) which handles multidimensional DSA in a kinetic solver. MAST is also one of the first codes that can take advantage of parallel computation or any scheme that subdivides the grid such as AMR, which greatly improves its ability to handle large multidimensional problems.

We will then use the solver detailed in Chapter 2 to do the first multidimensional combined magnetohydrodynamic (MHD) DSA models of the wind-embedded and the colliding wind binary scenarios. We couple the DSA solver to MHD instead of plain hydrodynamics because the CR diffusion length is dependant on the magnetic field. Thus to have a self consistent magnetic field, MHD is needed.

Since each scenario has its own unique features we will treat each in a separate chapter. First we will deal with the wind-embedded shock scenario in Chapter 3, then we will deal with the colliding wind binary scenario in Chapter 4. Finally a summary, conclusions, and future prospects from both the runs will be detailed in Chapter 5.

Chapter 2

Multidimensional Diffusive Shock Acceleration

As described in the Introduction a multidimensional DSA solver will be critical to our investigation of particle acceleration in stellar winds. To that end we describe our implementation of a multidimensional DSA solver in this chapter, and provide tests to show its robustness. In §2.1 we layout our numerical method and §2.2 we show one and two dimensional tests of our code.

2.1 Numerical Method

For kinetic diffusion solvers the governing equation is the diffusion-convection equation (DC) which describes the evolution of an isotropic (in momentum) CR distribution function, $f(x,p,t)$. Where x is the spatial location, p is the particle momentum, and t is time. The DC equation can be written in multiple dimensions as (e.g., Skilling (1975))

$$\frac{\partial f}{\partial t} + \vec{v}\cdot\nabla f = \frac{1}{3}(\nabla\cdot\vec{v})\frac{\partial f}{\partial y} + \nabla\cdot(\overleftrightarrow{\kappa}\cdot\nabla f) + \frac{1}{p^3}\frac{\partial}{\partial y}\left(pD\frac{\partial f}{\partial y}\right) + S \qquad (2.1)$$

where v is the bulk flow speed, $y = ln(p)$, $\overleftrightarrow{\kappa}$ is the spatial diffusion tensor (we will assume here that it is purely diagonal and isotropic), D is the momentum diffusion coefficient, and S is a representative source function. Henceforth we will express the

particle momentum in units of $m_p c$.

Typically eq. (2.1) is solved in conjunction with the evolution of the MHD flow. This interaction with the MHD fluid comes via a back pressure provided by the CRs, P_c, which is defined as

$$P_c = \frac{4\pi}{3} m_p c^2 \int_{p_{min}}^{p_{max}} p^4 f \frac{dp}{\sqrt{1+p^2}} \tag{2.2}$$

Since the CR pressure is dependent on the CR mass, contributions to the CR pressure from electrons will be ignored. The CR pressure is applied to the MHD equations, detailed in §2.1.4 by modifying the momentum and energy terms in the following way

$$\begin{aligned} \frac{\partial \vec{v}}{\partial t} + \vec{v} \cdot \nabla \vec{v} + \frac{1}{\rho} \nabla (P_g + P_c) - \frac{1}{\rho} (\nabla \times \vec{B}) \times \vec{B} = 0 \\ \frac{\partial P_g}{\partial t} + \vec{v} \cdot \nabla (P_g + P_c) + (\gamma_g P_g) \nabla \cdot \vec{v} = -L(x,t) \end{aligned} \tag{2.3}$$

Where $L(\vec{x}, t)$ accounts for the energy lost via injection of particles from the thermal gas into the CRs. Terms due to the CR inertia are neglected in such computations as the mass fraction of CRs is generally very small.

As noted in Chapter 1, the heating and compression due to the CR precursor can lead to substantial changes in the strength of the dissipative, gas subshock and to the postshock conditions relative to those in a pure gas dynamic shock of the same Mach number. Given these flow modifications in front of the subshock, it is helpful for the sake of later discussion to identify specifically the unmodified, upstream conditions by the subscript '0', the conditions immediately upstream of the gas subshock by the subscript '1', and the conditions immediately downstream of the full shock structure by the subscript '2'.

The multidimensional solution of the combined MHD-CR equations can be done in an operator and dimensionally split manner. Thus the multidimensional form of eq. 2.1 can be reduced down to the one dimensional form that utilizes a scalar diffusion coefficient. The first term on the right hand side (RHS) of eq. (2.1), the momentum convection term, is solved using the CGMV method (§2.1.1). The second term on the RHS of eq. (2.1), the spatial diffusion term, is solved using the MAST method (§2.1.2). The third term on the RHS of eq. (2.1), the momentum diffusion term, is only important

for second order Fermi acceleration which is not treated in this thesis and as such will be neglected. The final term on the RHS of eq. (2.1), the source terms, deals with particle injection which is discussed in §2.1.3 and energy losses which are discussed in Appendix A. Finally the MHD solvers used in tandem with the CR solvers are discussed in §2.1.4.

2.1.1 CGMV

CGMV is used to reduce the computational expense of the DSA simulation. We will provide a brief description of CGMV, the full treatment can be found in Jones & Kang (2005). It is well known that powerlaw CR spectra are common in most astrophysical situations. CGMV leverages this by assuming that the CR spectrum will inherently be a piecewise powerlaw in momentum. Utilizing this assumption one can solve the DC equation using two moments of the CR distribution function n and g which are defined as follows

$$n_j = \int_{p_j}^{p_{j+1}} p^2 f(p) dp, \qquad g_j = \int_{p_j}^{p_{j+1}} p^3 f(p) dp. \tag{2.4}$$

Where j is the momentum bin index. One can then treat the momentum convection term similarly to how one would treat any upwinded finite volume convection problem. This formulation allows for the solution of the DC equation with an order of magnitude less momentum bins than conventional solvers. The resulting reduction to the amount of computational time via the reduced number of momentum bins makes the DSA time step roughly the same order as the MHD time step. The results of solving the momentum convection using CGMV have been shown to agree well with conventional solvers, in spite of the reduced momentum resolution of CGMV.

2.1.2 MAST

While CGMV allows for the solution of the momentum convection, the spatial diffusion still needs to be accounted for. In Jones & Kang (2005) the spatial diffusion was solved via the second order, semi-implicit Crank-Nicolson (CN) scheme by a tridiagonal solver of the following form for n at momentum bin j and spatial bin i for time step t^k, the solver for g is similar in form,

$$
\begin{aligned}
A_i^+ n_{i+1}^{k+1} + A_i^0 n_i^{k+1} + A_i^- n_{i-1}^{k+1} &= C_i^0, \\
K_{i,j} &= \frac{\int_{p_j}^{p_{j+1}} \kappa_i f_i p^2 dp}{n_{i,j}} \\
K_{i+1/2} &= \frac{K_{i+1} + K_i}{2}, \\
A_i^+ &= -\delta K_{i+1/2}, \\
A_i^0 &= 1 + \delta(K_{i+1/2} + K_{i-1/2}), \\
A_i^- &= -\delta K_{i-1/2}, \\
C_i^0 &= n_i^k [1 - \delta(K_{i+1/2} + K_{i-1/2})] \\
&+ n_{i+1}^k \delta K_{i+1/2} + n_{i-1}^k \delta K_{i-1/2} + \Delta t^k F_i,
\end{aligned} \tag{2.5}
$$

Where $\delta = (1/2)\Delta t^k/(\Delta x)^2$ with Δt^k being the time step size and Δx the spatial zone width. $K_{i+1/2}$ is the diffusion coefficent at the zone boundary averaged over the momentum interval $p_j < p < p_{j+1}$. F_i includes the solutions for the fluxes for the momentum convection from the CGMV method and terms for particle injection. A cylindrical version of this is laid out in Appendix B

For 1-D problems the tridiagonal solver is an efficient way to solve the diffusion problem as the amount of work to integrate the entire grid is comparable to the MHD step. However in multiple dimensions the number of zones to be solved gets large requiring parallel computation. Normally parallel computation, or for that matter AMR, requires the division of the grid into smaller domains that are distributed to each processor. Dividing the grid in this manner effectively puts computational boundaries at the edge of each domain. This poses a problem for the tridiagonal solver as it is sensitive to boundary information due to its implicit nature. If used without modification for problems with short diffusion time scales the tridiagonal solver will create boundary artifacts which can lead to unphysical solutions.

The Multidimensional Adaptive Subcycling Tridiagonal (MAST) solver was developed to deal these issues. MAST modifies the tridiagonal solver such that it can be used in schemes that require the subdivision of the grid such as parallel computation and AMR. MAST has two primary components; adaptive subcycling and floating domain boundary conditions, both of which will be discussed in the next two sections.

2.1.2.1 Adaptive Subcycling

For typical diffusion coefficients used in DSA, especially those that increase with particle momentum, the length that a particle diffuses in a MHD time step can be a considerable portion of the computational grid. Normally the computational boundaries of the simulation are far enough away that a particle will not diffuse the entire length of the grid in one MHD time step. When the grid is subdivided into domains the diffusion length for particles on a particular domain can end up being much larger than the domain for the MHD time step, creating problems for the tridiagonal solver.

One can mitigate the problem by subcycling the tridiagonal solver. Subcycling works by dividing the MHD time step into even smaller time steps. The tridiagonal solver is then executed over these smaller time steps until the sum total of the subcycle time steps equals the MHD time step. This technique can be used to constrain the diffusion length for a given subcycle to be less than the length of the domain. However in certain cases this minimalistic constraint is not enough to maintain a physically reasonable solution. Physically unreasonable solutions manifest themselves as negative CR densities or pathological features which lead to negative CR densities. More subcycling can reduce and eliminate unphysical features. MAST accounts for this by allowing the subcycling to adapt itself to the evolution of the CR distribution.

The adaptive subcycling is executed as follows. The minimum number of subcycles, $n_{s,min}$, for a given domain and momentum is constrained to be

$$n_{s,min} = \frac{2\kappa_{max}(p)\Delta t}{l_d \Delta x}. \tag{2.6}$$

Where $\kappa_{max}(p)$ is the maximum diffusion coefficient at a given momentum for the domain, Δt is the MHD time step, Δx is the zone size, and l_d is the length of the domain. Note that the theoretical maximum number of subcycles needed for any domain, that required by an explicit solver, is given by taking $l_d = \Delta x$.

As the subcycling is executed the solver checks to see if the CR spatial distribution is still physically reasonable, after all the CN scheme is unconditionally stable but not always physically correct. Unphysical features typically result from sharp changes in the CR distribution around which the CN scheme tends to make oscillations. These oscillations start out on a small scale, only spanning a few zones with a small amplitude,

but over time they can grow and produce negative CR densities. If the solver detects this pathology in the distribution the solver stops the current subcycling. It then increases the number of subcycles to be executed and restarts the subcycling. The solver finishes when it makes it through all the subcycles without finding any pathologies.

2.1.2.2 Floating Domain Boundary Conditions

The constraint on subcycling in the previous section means that each domain and momentum will have a different amount of subcycling to accomplish. Synchronizing the domain boundaries becomes difficult in this case. Strict synchronization would require the amount of subcycles between all the domains to be the same, which is numerically inefficient. The number of subcycles would be constrained by the domain that required the largest number. Also, each domain would have to send boundary information for every subcycle. Doing both would be at least as inefficient as treating the entire grid in serial, probably more so. To preserve the benefits of parallel computation, one needs to minimize the number of synchronizations between domains and allow each domain to act independently.

MAST synchronizes boundaries at the beginning and end of subcycling. This can cause issues for the tridiagonal solver as it is highly dependent on the boundary information and sensitive to sharp features even with subcycling. To illustrate this problem, let us consider two examples. The first is where a considerable number of particles will diffuse off the domain in a MHD time step. The other will be the inverse case where an adjacent domain is feeding particles into the current domain.

The first case is illustrated in Figure 2.1. The top panel shows the initial distribution on the domain (solid line) and boundary (long dashed) along with what the ideal final solution (short dashed) would look like with no internal boundaries. Normally if the domain boundary were not present the values that would occupy the boundary zones would also increase as material diffused into them. Therefore using the boundary information acquired from synchronization of the grid will not be consistent with what the distribution naturally wants to do. The second panel illustrates what might happen by maintaining the boundary values acquired from initial synchronization. The final distribution (solid) is discontinuous with the boundary (long dashed), even worse the distribution has picked up an oscillation due to the discontinuity.

As a solution to this problem MAST utilizes floating boundary zones, illustrated in the third panel. The initial distribution and boundary are shown as long dashed lines. In MAST the boundary region is treated as a transition layer between the physical domain and the data contained in the boundary. The transition layer consists of all the boundary zones excluding the furthest boundary zone from the domain. The values for the transition layer are set by making a linear fit between the first zone on the domain and the furthest boundary zone from the domain, illustrated by the dotted lines in the boundary. The fit is recomputed every subcycle with the boundary value furthest from the domain being fixed in value for all subcycles. This linear transition layer inherently maintains the continuity of the distribution on the domain with the boundary. By using the furthest boundary zone as a pivot and allowing the boundary to float, it gives the distribution on the computational domain knowledge about the information in the adjacent domain without creating a discontinuity. Hence the final distribution (solid) closely approximates the ideal solution and is free from pathological boundary artifacts.

The second case is illustrated in Figure 2.2. The first panel in Figure 2.2 is similar to the first panel of Figure 2.1 but this time for the situation where boundary information needs to move onto the domain. As illustrated there is no guarantee that the information on the boundary will be continuous with the information on the domain. As shown before discontinuities in the distribution, even at the boundary, can cause oscillations as illustrated in second panel. MAST with its floating boundaries allows for the information to smoothly diffuse onto the grid as shown in the third panel. The long dashed line shows the initial distribution. Similarly to the previous case the distribution in the boundary is recalculated with a linear fit which smoothly connects the boundary with the distribution on the domain, illustrated by the dotted line. As solver subcycles information from the boundary propagates onto the grid. As this occurs the boundary is allowed to increase as well, maintaining a smooth transition. This allows the information on the grid to smoothly incorporate the information in the boundary without creating pathological boundary artifacts. As in the previous case the final distribution (solid) closely approximates the ideal solution (short dashes).

This solution does not strictly give the same answer as treating the entire domain via the standard tridiagonal method. This is because the boundary information used for the solution is at least one MHD time step old and particles may diffuse over multiple

domains. However, as we will show in §2.2, MAST produces a physically reasonable answer that is approximately the same as the standard method both in CR spectrum and spatial extent.

2.1.2.3 Domain Boundary Depth

The actual physical extent of the boundary in MAST is defined by the maximum diffusion length of the CRs at that momentum for that time step on the domain

$$l_{dif} = \frac{\kappa_{max}(p)\Delta t}{\Delta x} \tag{2.7}$$

The maximum size of the boundary is constrained to be no larger than the domain size. Utilizing this boundary depth criteria reduces the amount of subcycling needed by the solver. The larger boundaries makes the change in slope from the boundary to the grid less dramatic decreasing the chance of seeding unphysical features on the grid. It also allows the solver more information about what is going on in the adjacent domain so that the distribution can better adapt to the adjacent conditions.

However this additional speed up tends to make the edges of the domains show up more prominently in the CR distribution, though the edge effects are limited to the region immediately surrounding the boundary (as shown in §2.2.2). This is due to the one MHD time step delay in the boundary information. The edge features can be decreased by reducing the boundary size down to the minimum size needed for the CN scheme. Unfortunately the speed benefits of having the large boundaries, a reduction in computational time of about an order of magnitude versus the minimum boundaries, are lost by doing this. So it is a trade off of whether one needs the calculation to be completed more quickly or if one wishes to have a distribution mostly free of domain edge effects.

2.1.3 Injection

Injection is handled via a simple flux fraction model. In this model a small, fixed fraction of the thermal particle flux through the gas subshock, ϵ_{inj}, is injected at a momentum $p_{inj} = \alpha c_{s_2}$, where α is a constant greater than unity and c_{s_2} is the plasma sound speed immediately downstream of the subshock (e.g. Jones & Kang (2005)). We will set

$\alpha = 2.0$ for this simulation, which is the commonly accepted value (Jones & Kang 2005). This gives a source term for the DC eq. of $S(p) = \epsilon_{inj}(\rho_1/(\mu mp))u_s w(x-x_s)\delta(p-p_{inj})$, where ρ_1 is the gas mass density just upstream of the subshock, μ is the mean molecular weight, u_s is the subshock speed with respect to the plasma immediately upstream, x_s is the location of the shock center, and w is a normalized weight function that allows the injection to be distributed across the numerical shock structure. This distribution is put in place in order to prevent discontinuities in the CR distribution. The energy extracted from the thermal plasma is simply $L = \frac{1}{2}\epsilon_{inj} w(x)\alpha^2 c_{s_2}^2 \rho_1 u_s$.

2.1.4 MHD Codes

In multiple dimensions the equations for ideal MHD are

$$\begin{aligned}
\frac{\partial \rho}{\partial t} + \nabla \cdot (\rho \vec{v}) &= 0 \\
\frac{\partial \vec{v}}{\partial t} + \vec{v} \cdot \nabla \vec{v} + \frac{1}{\rho}\nabla P_g - \frac{1}{\rho}(\nabla \times \vec{B}) \times \vec{B} &= 0 \\
\frac{\partial P_g}{\partial t} + \vec{v} \cdot \nabla P_g + \gamma_g P_g \nabla \cdot \vec{v} &= 0 \\
\frac{\partial \vec{B}}{\partial t} - \nabla \times (\vec{v} \times \vec{B}) &= 0 \\
\nabla \cdot \vec{B} &= 0
\end{aligned} \tag{2.8}$$

Where ρ is the gas mass density, v is the velocity, P_g is the gas pressure with $P_g \propto \rho^{\gamma_g}$, γ_g is the gas adiabatic index, and B is the magnetic field. Two different MHD codes are used in this paper to demonstrate the effectiveness of MAST. The first is AstroBEAR (Astronomical Boundary Embedded Adaptive Refinement), an AMR code, and the second is WOMBAT (sWift Objects for Mhd BAsed on Tvd), a fixed grid code. Each are discussed in the next two sections.

2.1.4.1 AstroBEAR

We will only provide a brief overview of AstroBEAR here, for a complete description see Cunningham et al. (2009). AstroBEAR solves the MHD equations utilizing a MUSCL (Monotone Upstream-centered Schemes for Conservation Laws) type solver along with

a version of the Constrained Transport scheme described in Ryu et al. (1998) which has been modified for AMR.

The AMR patches are normally placed where gradients in the MHD variables are significant. For MAST the normal refinement criteria are expanded to include refinement on the gradients of the CR distribution and around shocks. Regions surroundings shocks are refined to level required for a converged solution, $\Delta x < 0.1 l_p$, for which $l_p = \kappa / u_s$ is the characteristic precursor diffusion length (Jones & Kang 2005). This region is refined out to at least one diffusion length at the injection momentum.

For the refinement of the gradients of the CR distribution the maximum allowed refinement is defined by which CR momentum is most important in that region, decided by the CR density and gradient. As noted in the previous paragraph the minimum resolution necessary for a converged CN solution is $\Delta x < 0.1 \kappa / u_s$. The domain in question may not know what the shock velocity is for the CRs on the domain, which could be from multiple shocks on separate domains. Because of this we opt to use the characteristic diffusion length (eq. 2.7), l_d, of a particle over a dynamical time, achieved by setting Δt to 1. Close to shocks the resolution needs to be the highest as it is dominated by low momentum CRs. However further from shocks the resolution required declines as higher momentum CRs dominate. AstroBEAR takes this into account when deciding which regions to refine.

2.1.4.2 WOMBAT

WOMBAT is a highly parallel hybrid fixed grid MHD solver. Based off the TVD (Total Variation Diminishing) MHD formulation of Ryu & Jones (1995); Ryu et al. (1995, 1998) this new implementation was coded by Peter Mendygral at the University of Minnesota. WOMBAT has been shown to scale perfectly up to thousands of processors and has a small memory footprint per processor[1] . This gives it a distinct advantage over AstroBEAR which currently has a large memory footprint per processor and is inherently more difficult to parallelize owing to its AMR structure. The disadvantage of WOMBAT for these type of problems is its fixed grid nature which over resolves large portions of the grid.

[1] Visit http://www.astro.umn.edu/groups/compastro/ for more details

2.2 Discussion

2.2.1 1-D Test

We first do a comparison between the solver presented in Jones & Kang (2005) and the MAST solver for a 1-D shock structure. The shock is a standing Mach 30 shock (adiabatic index, $\gamma = 5/3$) with the incoming flow from the right side of the grid having $\rho = 1$, velocity of $v = 1 = 0.01c$, upstream sound speed of $c_s = \frac{1}{30}$, and upstream Alfvén velocity of $v_A = \frac{1}{10000}$ with the magnetic field being parallel to the shock normal. The magnetic field is kept weak in this test to allow us to focus solely on the DSA and CR feedback. The grid has a physical extent of $-50 < x < 50$. We use continuous boundary conditions for both the MHD and DSA solvers at the physical edges of the grid. These boundary conditions use the zones adjacent to the physical boundary as the values in the boundary zones. The shock is positioned at $x = 0.5$. An isotropic Bohm-like diffusion coefficient is used where $\kappa = 1.0p$. Normally this would be dependant on the magnetic field magnitude and direction. However as that would complicate the test we will neglect the effects of the magnetic field on the diffusion. Fourteen momentum bins logarithmically span the range between $0.000912 < p < 1097$. With this shock velocity, the injection momentum is $p_{inj} = .01$, which means we will use a resolution of $\Delta x = 0.0015625$. The injection fraction is set to $\epsilon_{inj} = 1 \times 10^{-4}$ and CR feedback is included as well. For the Jones & Kang (2005) solver the run is computed using the standard CN scheme where as WOMBAT utilizes the MAST solver with 16 domains distributed evenly across the computational grid. This simulation was run out to $t = 40$.

Figure 2.3 shows the results at the final time. The left plot shows the spatially integrated spectrum $G(p) = \int g(p)dx$ for both the Jones & Kang (2005) solver and the MAST solver. The right plot shows the cosmic ray pressure distribution for both solvers and the domain boundaries for the MAST run.

Starting with the left plot the distributions are essentially the same below the high energy turn over with a fractional error less than 2%. At the high energy turn over the spectrum changes quickly which is where the maximum fractional error between the two spectra occurs, which is no larger than $\sim 25\%$. The right plot shows that the MAST distribution of CR pressure is free of obvious boundary artifacts but is reduced by $\sim 5\%$. This reduction can be attributed to the fact that MAST behaves as if it is

slightly less diffusive than Jones & Kang (2005). This reduction in the diffusion is due to subdividing the grid. As noted before the boundaries are only synchronized before and after MAST is executed. This has two effects, first it limits the particle diffusion length between synchronizations to the domain size. Second it lowers the effective "pressure" on the distribution to diffuse as the boundary data is not the most recent. MAST mitigates some of these effects by utilizing floating boundaries but it does not remove all of them. The lower effective diffusion reduces the number of particles sent upstream of the flow to participate in acceleration. This in turn causes the decrease in CR pressure. The reduction in CR efficiency can be compensated for by increasing the CR injection.

Still the solutions have nearly the same spectrum and the pressures have similar distributions in spite of the offset. This shows that MAST can solve the kinetic DSA problem with multiple patches, and the solutions will be approximately the same as the standard solvers. The subcycling in this case took its toll on the execution of the run. The MAST solver in this case increased the length of time for the execution of the run by an order of magnitude over the Jones & Kang (2005) solver. While not as good of performance as the Jones & Kang (2005) solver it does allow the subdivision of the grid and use of multiple processors.

2.2.2 2-D Tests

To show the effectiveness of MAST in 2-D we have constructed standing shocks of the same type as the 1-D test but now tilted at 45^o and 20^o and excluding CR feedback. A smaller grid was used for this run, $-1 < x, y < 1$ netting to 1280^2 in size. As in the 1-D test both the MHD and DSA solvers use continuous boundary conditions at the physical edge of the grid. The simulation was run out to $t = 0.5$. The simulations were done using WOMBAT and AstroBEAR. The WOMBAT runs were executed using 1 large domain, 4 domains arranged 2x2, and 16 domains arranged 4x4. The AstroBEAR runs were done with 3 levels of refinement above the base level which had a resolution of 160^2.

Figures 2.4-2.6 show the results for the 45^o case. Figure 2.4 shows a plot of the log of the density at the final time with the AstroBEAR mesh overlaid in blue, and the magnetic field overlaid in red. The features propagating in from the edge are due to the

fact that the grid does not have infinitely deep boundaries. Thus the shock does not look like an infinite plane but rather a shock of finite extent. Still at $t = 0.5$ the middle of the shock has not been effected by the boundaries yet and still looks similar to a Mach 30 standing shock. Figure 2.5 shows a line cut of the spectrum at the center of the shock for all of the cases, the 1-D solution is included for reference. We will compare against WOMBAT 1 as it contains the full 2-D nature of the problem and uses the standard solver in a dimensionally split manner. The maximum fractional error between all of the spectra is $\sim 40\%$. All the WOMBAT spectra overlay each other within $\sim 10\%$.

Figure 2.6 shows the CR spatial distribution for $p = 0.05$. The distributions generally look the same. However in detail edge artifacts are visible for the 4 and 16 domain case. These are also present for the AstroBEAR case but the domains are small and as such are hard to see on the image. Still the AstroBEAR distribution does look cleaner than the 4 and 16 domain case for WOMBAT. This is due to a difference in the boundary depth used for AstroBEAR and WOMBAT. AstroBEAR has a boundary depth of 4 zones for all of its meshes where as WOMBAT has a variable boundary depth as defined in §2.2.3. As discussed in §2.2.3 the variable boundary depth has a faster execution than the smaller boundary depth but the answer does tend to show edge effects more prominently. Nonetheless the edges only effect their immediate surrounding and not the larger morphology.

Figures 2.7-2.9 show the analogous run for 20^o. This case is a more difficult test as the velocity jump seen in the y direction is 36% that seen in the x direction unlike the 45^o case which has equal velocity jumps in x and y. As can be seen from Figures 2.8 and 2.9 the distributions are approximately the same at a similar level as the 45^o case. Thus MAST can handle a shock of any orientation to the grid without suffering directionally dependent effects.

2.3 Summary

Multidimensional effects can dramatically change the evolution of the flow, which impacts the evolution of the CR population. MAST is the first solver that handles multidimensional kinetic DSA. As demonstrated above the MAST solver produces results approximately the same as normal kinetic solvers in one and two dimensions. This

allows for the exploration of more complex multidimensional flows with the benefits of parallel computation and AMR.

MAST has its limitations, as it is only an approximate solution. The CR distributions derived from MAST are similar in spectral shape, distribution shape, and magnitude to standard kinetic solvers. The approximate nature of the solution is the trade off for MAST in allowing subdivision of the grid. The additional cost to solve DSA using MAST is about an order of magnitude more than the Jones & Kang (2005) solver. While not as efficient as the solver described in Jones & Kang (2005) it does allow for multidimensional and multiprocessor DSA calculations.

MAST opens the door for DSA simulations of a wide array of astrophysical systems. In the next chapters we will use MAST in combination with WOMBAT to model wind-embedded shocks in O-star winds and colliding wind binaries in multiple dimensions.

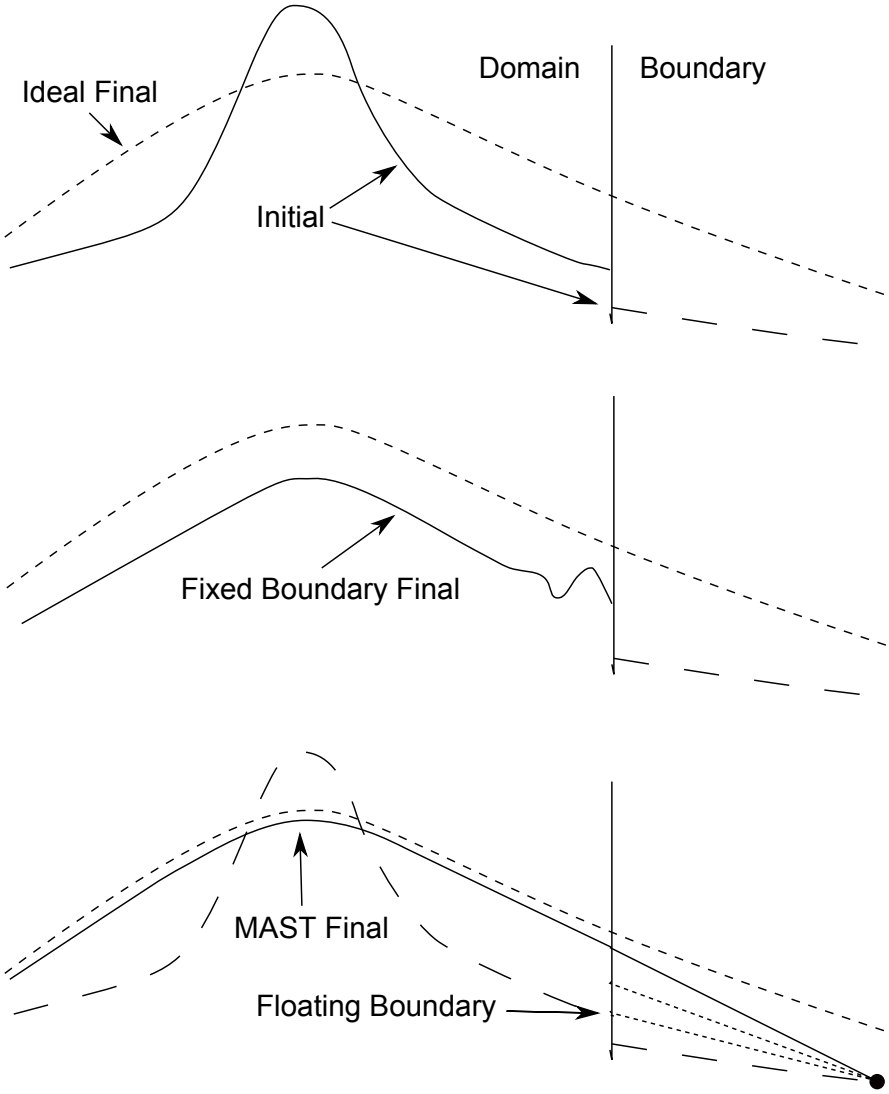

Figure 2.1: Illustration showing what happens when particles diffuse off a domain in a fixed boundary solver versus the MAST floating boundary solver.

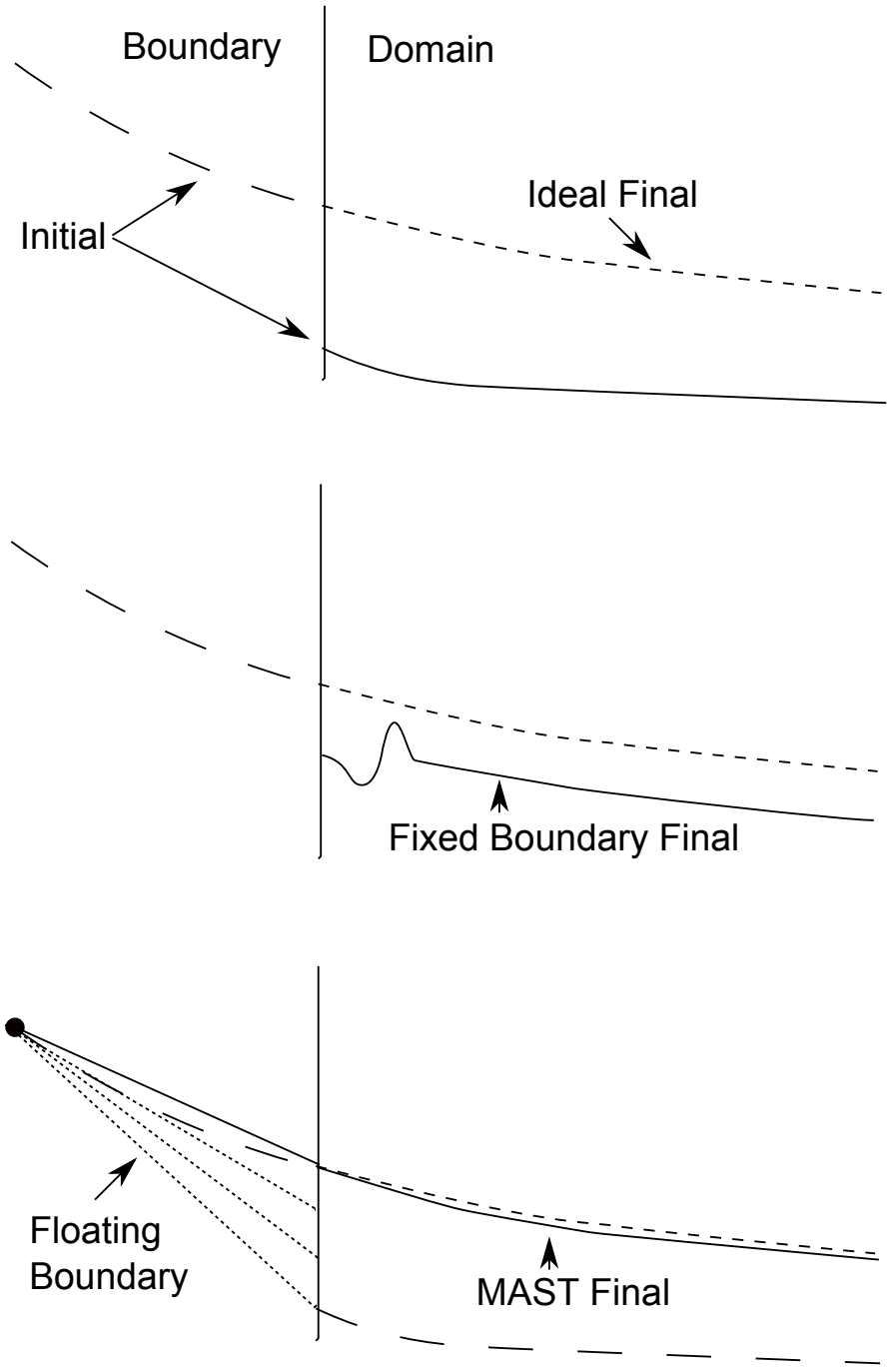

Figure 2.2: Illustration showing what happens when particles diffuse on to a domain in a fixed boundary solver versus the MAST floating boundary solver.

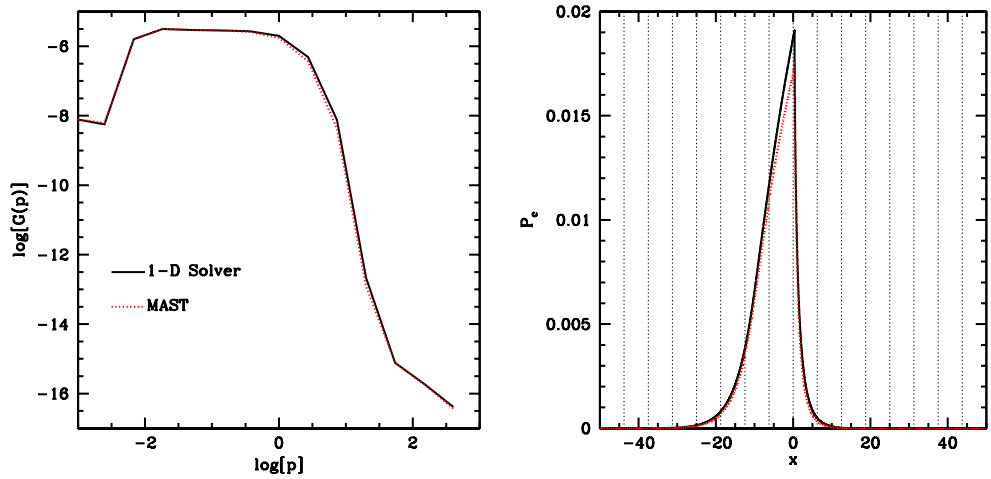

Figure 2.3: Left: Spatially integrated spectrum for 1-d solver for the entire grid and MAST in WOMBAT with 16 domains. Right: Cosmic Ray Pressure distribution for 1-d solver for the entire grid and MAST in WOMBAT with 16 domains. The vertical dotted lines represent the domain boundaries in the MAST run.

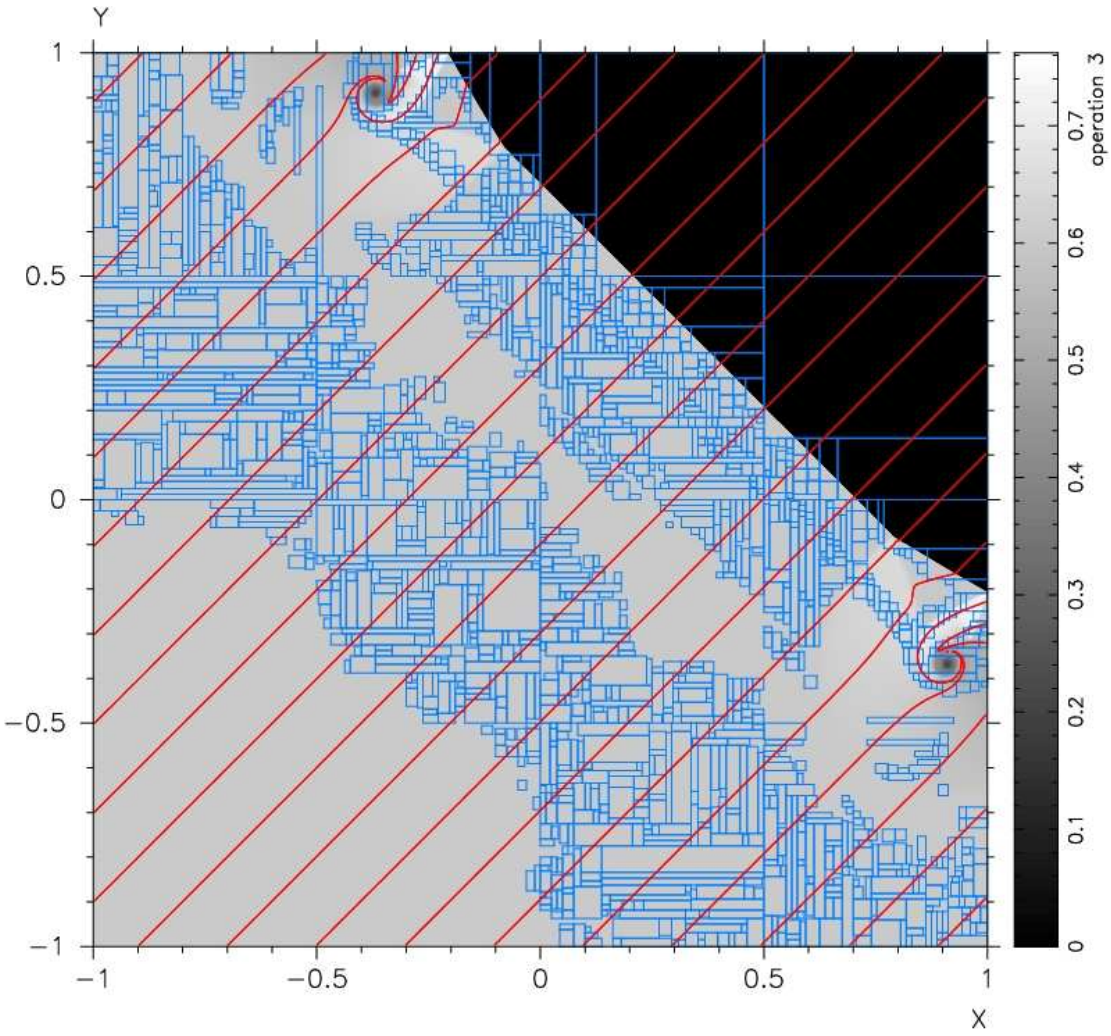

Figure 2.4: Log of Density for 45 degree shock at $t = 0.5$. Red lines are magnetic field orientation. Blue lines are the mesh for AstroBEAR.

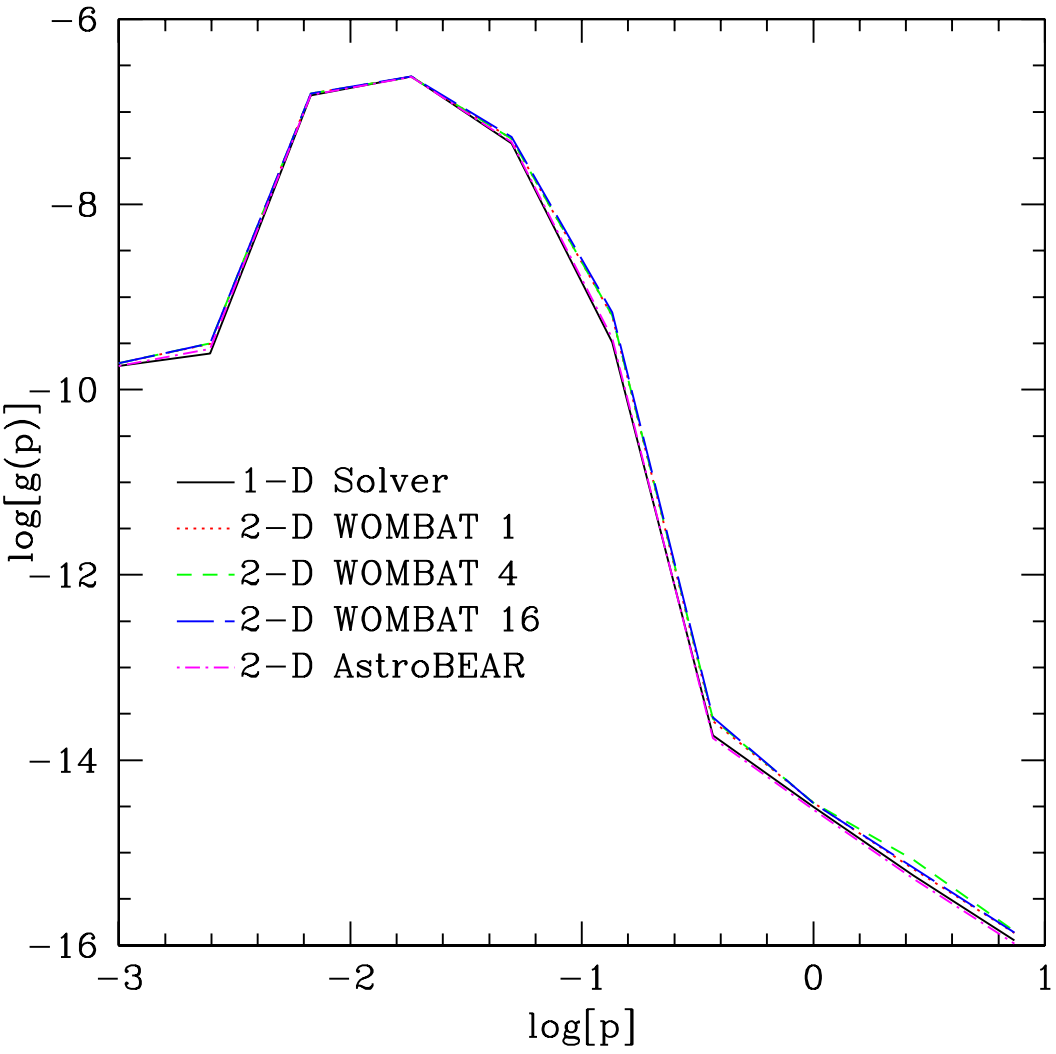

Figure 2.5: Spectrum at 45 degree shock at $t = 0.5$.

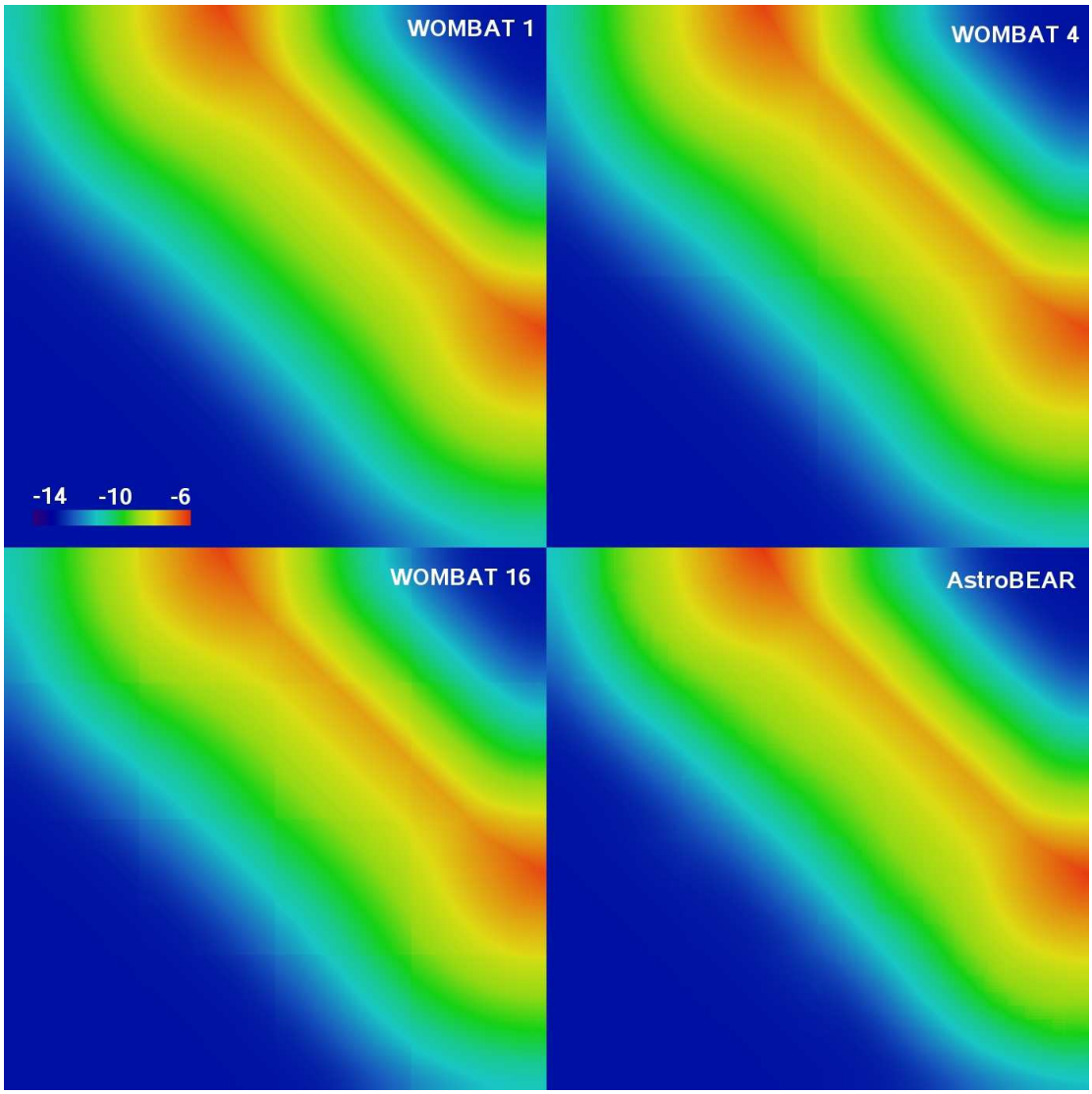

Figure 2.6: $log(g(p))$ at $p = .05$ for a 45 degree shock at $t = 0.5$.

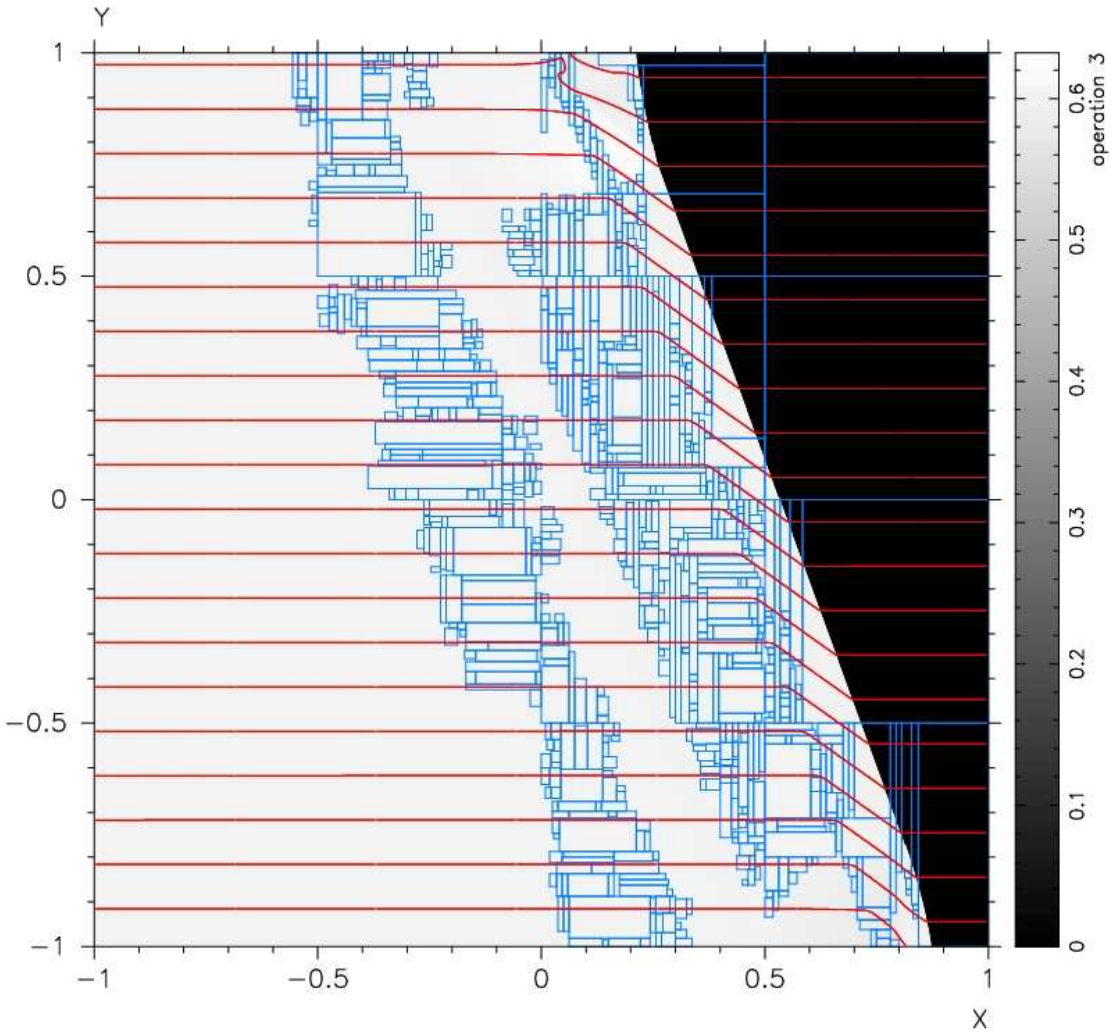

Figure 2.7: Log of Density for 20 degree shock at $t = 0.5$. Red lines are magnetic field orientation. Blue lines are the mesh for AstroBEAR.

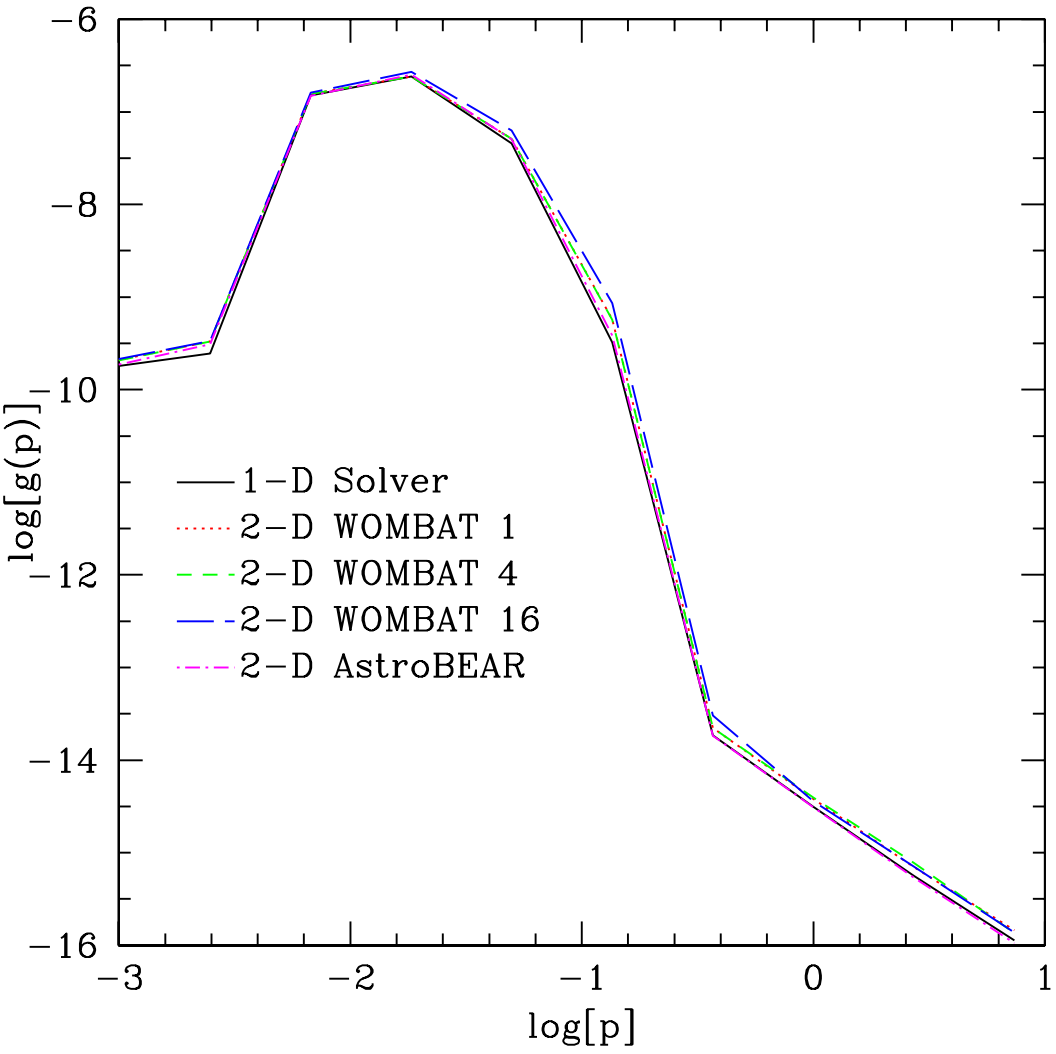

Figure 2.8: Spectrum at 20 degree shock at $t = 0.5$.

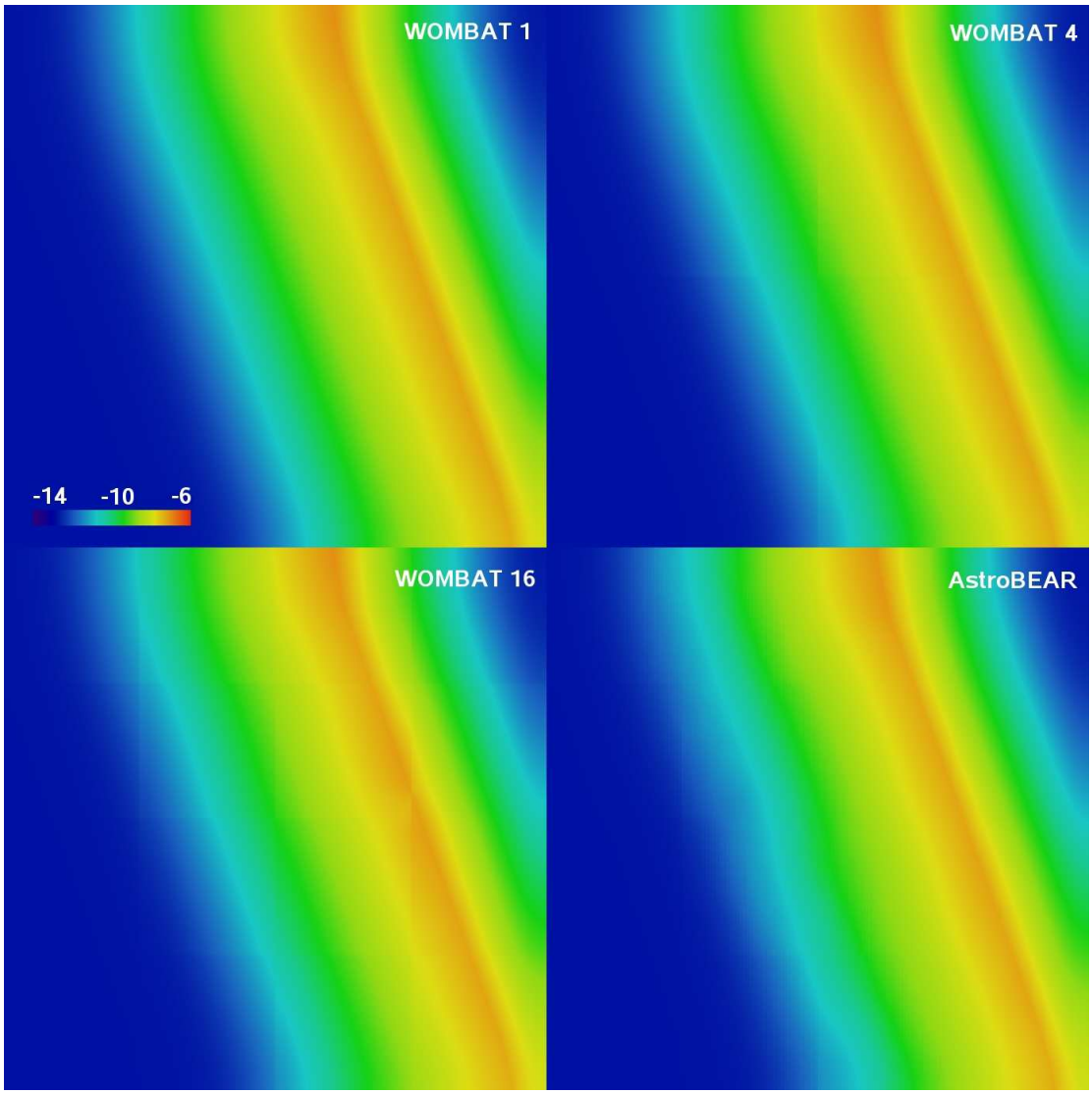

Figure 2.9: $log(g(p))$ at $p = .05$ for a 20 degree shock at $t = 0.5$.

Chapter 3

Multidimensional DSA at Wind-Embedded Shocks in O-star Winds

Now that we have a solver that is capable of treating multidimensional DSA, we will now consider the problem of modeling wind-embedded shocks around a single O-star. As noted in Chapter 1, this scenario is currently disfavored as the explanation for the nonthermal emission from O-stars. However, in order to fully rule out this scenario full DSA modeling must be undertaken. In §3.1 we will lay out our simulation set up and in §3.2 we will discuss the results of the simulation.

3.1 Numerical Method

The dynamics governing the line driven instabilities that lead to wind-embedded shocks around O-stars are complex as noted in Chapter 1. The added complexity of DSA makes a fully consistent treatment of these systems computationally prohibitive. To simplify the problem we will model the stellar wind and instabilities after they reached their asymptotic form. Given these simplifications we neglect the gravity of the star and radiation driving, as they only play a role in the wind dynamics when the wind is being accelerated. Radiative heating and cooling can still be important in the wind

dynamics. Unfortunately, the code we will use does not incorporate these dynamics robustly. However, we can approximately account for the dynamical effects of these processes as described in §3.1.2. We will discuss the particulars of MHD-DSA solver used for this simulation in §3.1.1 and in §3.1.2 we layout the initial conditions for this simulation.

3.1.1 MHD-DSA Solver

We will use the DSA solver described in Chapter 2 in conjunction with the WOMBAT MHD solver. While WOMBAT can handle 3-D MHD simulations, we will limit ourselves to modeling the wind in 2.5-D cylindrical coordinates (Ryu et al. 1995). In 2.5-D cylindrical coordinates we assume symmetry around the z axis. However, the velocity and magnetic field components in the ϕ direction still affect the flow dynamics. Unfortunately, 3-D simulations are still prohibitively expensive for DSA-MHD simulations. Thus 2.5-D cylindrical coordinates allows us to simulate the wind in an approximately 3-D manner.

3.1.2 Simulation Setup

Generally O-stars have wind structures that are largely independent of the mass of the star (Lamers & Cassinelli 1999). As such we will model a representative 22 $M_\odot$ O-star which has a radius $R_s = 8.5$ $R_\odot$ and luminosity of 2.3×10^5 $L_\odot$ (Table 3.1 contains the simulation parameters). Since we do not include gravity or radiation physics needed to self consistently model the wind acceleration we will treat the wind when it reaches its asymptotic limit. This typically happens around 10 R_s for O-stars, with an asymptotic velocity of 2000 km/s and mass loss rate of $\dot{M} = 10^{-6}$ $M_\odot$/yr (Lamers & Cassinelli 1999).

The wind temperature is maintained at 10^4 K due to photoionization from the star's ultraviolet (UV) flux which prevents the wind from cooling as it expands (Lamers & Cassinelli 1999). The wind is not only heated due to the radiation flux from the star but strong metal lines cool the gas when heated above 10^4 K (Kholtygin et al. 2003). The shocks generated by the line driving instability are affected by strong cooling as well (Runacres & Owocki 2002). The heating and cooling length for the winds and shocks

we will model here is shorter than any distance we can feasibly resolve computationally. The combined rapid heating and cooling of the wind to 10^4 K makes the wind behave isothermally rather than adiabatically. As such we will treat the wind as an approximately isothermal fully ionized proton-electron plasma ($\gamma_g = 1.001$). We will also enforce this fact when the CR pressure and injection energy losses are applied to the ambient medium.

The strength of the magnetic field around O-stars is not well known as few measurements exist (Donati & Landstreet 2009; Kholtygin et al. 2010). However those that are detected, presumably those with the strongest field, have a surface magnetic field strength in the range of $100 - 1000$ Gauss (Donati & Landstreet 2009; Kholtygin et al. 2010). We will use a magnetic field strength at the surface of the star of 10 G. This value, based on observational completeness arguments, should be representative for many O-stars (Kholtygin et al. 2010). This is important as radio observations show that a quarter of observed O-stars show nonthermal emission. The high frequency of nonthermal radio detection indicates that whatever is causing the emission is not limited to exceptional systems. A surface magnetic field strength of 10 Gauss also lies in the theoretical range of expected magnetic fields for nonthermal emitting stars (van Loo et al. 2004).

The actual geometry of the field is observationally unknown. O-stars are thought to have a simple magnetic field configuration of a rotating radial field (Lamers & Cassinelli 1999). Rotating stars, such as our own Sun, bend their radial fields into the azimuthal direction due to the drag of the field lines frozen into the wind (Lamers & Cassinelli 1999). In this case we assume the azimuthal component is dominant compared to the radial component. This has the advantage of allowing us to ignore the radial field, which is difficult to model numerically. We use the following magnetic field in spherical coordinates,

$$\vec{B} = B_s \frac{v_{rot}}{v_w} \left(\frac{R_s}{R} \right) H(\theta) \hat{\phi} \tag{3.1}$$

Where B_s is the magnetic field at the surface of the star, R is the radius, v_{rot} is the rotational velocity of the star, and v_w is the wind velocity. $H(\theta)$ is a function that has a value of 1 for a polar angle θ greater than 90^o and a value of -1 below 90^o. This

direction change is caused by the requirement that the radial field, which the azimuthal field is derived from, be divergence free. For O-stars there is no corelation between the magnetic field strength and rotational velocity as there is for other types of stars (Donati & Landstreet 2009). As such we use a stellar rotational velocity of 25 km/s which gives a rotational period of 17.2 days. This will bend the field into a dominantly azimuthal field by the wind radii modeled here.

The line-driven instabilities are modeled to be similar to those produced by (Owocki 2009). We do not model the development of the instability. Rather we take the asymptotic form and put it into the ambient wind flow. The instabilities are constructed such that they preserve the kinetic energy density of the wind at the location where they are injected. Simulations of the development of the instabilities show that the maximum velocity jump is about 50% of the wind velocity (Owocki 2009). The form of the instability is a high velocity, low density region interior to a low velocity, high density region (see Figure 2.1) (Owocki 2009). These instabilities are well developed by the time the star's wind goes asymptotic (Runacres & Owocki 2002; Owocki 2009). As such we will use a driving region radius of 50 R_s which places us firmly in the asymptotic wind, where the radiative driving of the wind and instabilities diminishes.

The size of the velocity jump from the ambient wind velocity is randomized in this calculation with the maximum set to 50% of the wind velocity. The instabilities are randomly generated in angular wedges around the driving region, each $\pi/32 \sim 5.5^o$ in angular extent. The randomization of the velocities and positions of the instability is justified as the seed for the instability are random velocity fluctuations in the wind. The instabilities are injected in to the flow at the outer boundary of the driving region with the instabilities themselves being $4R_s$ in radial extent. The frequency, angular extent, and placement of the wedges are designed to mimic the clump model used by (Hamann et al. 2009) to explain X-ray emission from O-stars (see Figure 2.2). After the instability is injected it is free to evolve as the MHD demands without any further driving.

The injection fraction for the electron and protons is set to $\epsilon_{inj} = 10^{-4}$ which is typical for most shock Mach numbers (Kang & Jones 2007). However since the electrons are passive they can be rescaled to any injection fraction. As noted in §1 it is

commonly thought that the CR diffusion is dependant on the gyroradius of the particle, r_g. As such we use an isotropic Bohm-like diffusion coefficient of $\kappa = \frac{1}{3} r_g c = \kappa_o \frac{p}{B} = 3.13 \times 10^{16} \frac{p}{B}$ cm^2/s where B is in Gauss (Blandford & Eichler 1987). We set the CR momentum range to span 14 momentum bins logarithmically spaced between $0.000912 < p < 1097$.

The electron population is allowed to suffer energy losses due to inverse Compton (IC) and synchrotron. Around O-stars the radiation field is highly anisotropic and contains a considerable number of ultraviolet photons. With such an extreme environment the full Klein-Nishina (KN) cross section becomes important in modeling of IC losses (see Reimer et al. (2006) for a full discussion). A full treatment of the effects of the KN cross section on the IC losses is very difficult and expensive to treat numerically. Reynolds (1982) showed that for a particle population that is isotropic in momentum, IC in a highly anisotropic photon fields is approximately the same as the isotropic case. That being the case we can safely assume isotropy to simplify the cross section. Unfortunately, even with this assumption the problem of including the KN cross section in the DSA calculation is computationally difficult. As such, we utilize the isotropic Thomson limit of IC for the sake of computational simplicity. This has the effect of over estimating the electron energy losses close to the KN limit. Thus any maximum electron energy that is derived from this simulation will be a lower limit. The radiation field for IC used falls off as $1/R^2$ away from the star. The energy losses for the protons are ignored as the threshold for energy losses due to photo-pair and photo-pion production in this environment is around 10^{14} eV. Energy losses due to proton-proton collisions are also not included as the losses are not significant over the timescale modeled here.

As noted above in §2.1.3 that the CR injection momentum is dependant on the immediate postshock sound speed. With the isothermal assumption we lose all information about what the normal adiabatic postshock sound speed would be. As such we use a fixed injection momentum of $p_{inj} = 0.01$ which is the characteristic injection momentum for shocks of moderate Mach Number (M $\sim$ 10). Jones & Kang (2005) noted that the resolution needed to create computationally converged solution is $\Delta x < 0.1 l_p(p_{inj})$, where l_p is the CR precursor length which is defined as $l_p = \kappa / u_s$ with u_s being the shock velocity. For our simulations we use a grid resolution of $\Delta x = 0.03125$ R$_s$, which meets the Jones & Kang (2005) criterion for a shock Mach number of 10 and a characteristic

magnetic field strength of 0.25 mG. As will be shown in the next section this Mach number ends up being the maximum Mach number for the shocks generated in this simulation. The spatial extent of the grid is $-200R_s < x < 200R_s$ and $0 < y < 200R_s$ giving a total box size of 12800×6400.

3.2 Results

3.2.1 CR Feedback in Isothermal Environments

We noted in the previous chapters that CR feedback can be an important factor in the evolution of the flow. However when we attempted to apply its effects in this simulation, we could not get the resulting flow to be numerically stable. The reason for this is due to the isothermal nature of the shocks and the dependence of the diffusion coefficient on the magnetic field.

With the magnetic field being azimuthal it behaves similarly to the density in terms of its compression. In isothermal shocks the compression ratio depends on the square of the Mach number. As such the magnetic field is dramatically enhanced at the shock. The high magnetic field in the postshock flow reduces the diffusion length and confines many of the CR particles to a very small region. Any particles that do manage to escape upstream are compressed by the shock again. This creates a very high local CR pressure which is restricted to the clump and thus cannot form a strong CR precursor. With out a strong precursor the incoming flow is not slowed and the shock is not weakened. Thus injection and particle acceleration do not change and the CR pressure continues to increase. Eventually the CR pressure becomes so high in the clump and the gradient of the CR pressure becomes so strong that it blows apart the clump violently. This is undesirable as it causes very large velocities to suddenly appear on the grid which cause numerical instability.

The fact that this occurred in our simulations indicates that we have not fully resolved the precursor in terms of its effects on the MHD. This is due to the precursor being much shorter than we expected due to the high magnetic field in the clump. Fully resolving the precursor would be computationally prohibitive, so we have opted to investigate the multidimensional DSA in absence of CR feedback. However, in light of this behavior and the importance of radiative cooling in astrophysical environments

further investigation into the dynamics of CR modified isothermal and radiative shocks in a simpler setting is warranted, which will be dealt with in a future paper. To our knowledge only two fluid models of the effects of CR feedback on these type of shocks have been performed and no investigations of full DSA including feedback at radiative and isothermal shocks exist (e.g., Wagner et al. (2006)).

3.2.2 MHD Evolution

An image of the logarithm of the gas number density can be seen in Fig. 3.3 at $t = 0.75$, where time is in units of R_s/c_s. Since the flow is isothermal and the magnetic field is azimuthal the pressure and magnetic field takes an analogous form to the density. One can see the development of the instabilities by following their evolution radially, as the instabilities are advected outward with the ambient wind as time progresses. The simulation is ended when the CR's accelerated by the clumps reach the edge of the grid.

The instabilities themselves develop in to dense clumps that travel slower than the wind. This is due to the low density, high velocity region of the instability running into the high density, low velocity region, which we will call from here on out the clump. A transmitted shock is formed at the interface that propagates through the clump. Without any radiative driving to sustain it, the high velocity region dissipates leaving the clump to interact with the ambient wind.

A simplified picture of the clump in its own rest frame can be seen in Fig. 3.4. For this discussion we will call the upstream region '1', the post bowshock region '2', the shocked clump region '3', and the unshocked clump region '4'. These subscripts are not related to the subscripts defined in Chapter 2 for use in discussing CR modified shocks, and are intended only for the present discussion. In the following discussion we will ignore the effects of the magnetic field as the plasma beta in the wind is around 300. For isothermal shocks the compression ratio across a shock is equal to the square of the Mach Number (Choudhuri 1998). Thus the bow shock will have a compression ratio of $\chi_B = \rho_2/\rho_1 = M_B^2$ where M_B is the bow shock Mach Number.

Our initial velocity perturbation has a maximum possible Mach number of 60. However, Figure 3.5 shows a histogram of the actual shocks that develop on grid which have Mach numbers in the range of 2-6. This drop in Mach number is a natural consequence of the initial clump formation. In the clumps the velocity of the post shock flow will be

reduced by a factor of the inverse Mach number squared. The initial dense region of the instability, which develops into the shocked clump, will at its slowest be moving at 50% of the flow velocity. When the clump develops the postshock flow, region 2, will roughly maintain this velocity as the transmitted shock does not impart much momentum to the clump itself. The resulting velocity jump between the preshock and postshock flow will the naturally give a Mach Number of roughly 8, not the original 60 the clump started at. While classically not strong shocks in the adiabatic sense, which is reserved for Mach numbers greater than 10, the clump bow shocks do have compression ratios significantly higher than the normal factor of four for adiabatic shocks. In fact any isothermal shock with a Mach number greater that 2 will have a compression ratio greater than 4, and will be considered strong in the adiabatic sense.

Between regions 2 and 3 in Fig. 3.4 there is a contact discontinuity which separates the post bowshock material and the shocked clump material. Normally for an adiabatic shock the contact discontinuity could have a density gradient but no pressure gradient. In isothermal clumps the requirement that there cannot be a pressure gradient across a contact discontinuity dictates that the densities across the contact discontinuity must be the same, thus $\rho_2 = \rho_3$.

This relation between region 2 and 3 then dictates the conditions for transmitted shock that separates regions 3 and 4. The transmitted shock Mach Number will go as $M_T = \sqrt{\rho_3/\rho_4} = \sqrt{\rho_2/\rho_4} = \sqrt{\chi_B/\chi_c}$ where $\chi_c = \rho_4/\rho_1$ is the density contrast ratio between the clump and the ambient wind. The clump crushing timescale then is just $\tau_{cc} = l_c/(M_T c_s) = l_c\sqrt{\chi_c}/(M_B c_s)$, where c_s is the sound speed and l_c is the radial clump size. To get a sense of how fast the cloud is crushed let us construct an example clump crushing time in the time units established above. The strongest bowshock expected is $M_B = 8$ and the largest clump contrast ratio is $\chi_c = 4$. Thus $t_{cc} = 0.25$ as compared to the entire simulation which goes for $t_{sim} = 0.75$. This means that the transmitted shock propagates through the clump quickly with respect to total length the simulation.

Normally one would expect instabilities such as Rayleigh-Taylor (RT) and Kelvin-Helmholtz (KH) to shred the clump. Rayleigh-Taylor instabilities are suppressed in the isothermal case as the pressure and density gradients are always aligned. Kelvin-Helmholtz can still occur at the contact discontinuity between the post bowshock flow and the shocked clump. This shear layer will have a characteristic velocity of the post

bowshock flow. Therefore the KH growth timescale goes as $\tau_{KH} = 2l_c/v_2 = 2\chi_B l_c/v_1 = 2l_c M_B/c_s$. Thus the ratio of the clump crushing time and the Kelvin-Helmholtz time is simply $t_{KH}/t_{cc} = 2M_B^2/\sqrt{\chi_c} = 2M_T M_B$. Since RT is suppressed and the KH timescale is longer than the clump crushing timescale by a factor M_B^2 this means that the clumps will remain coherent for a considerable amount of time before they are shredded. This is evidenced by the lack of clump disruption seen in Fig 3.3.

Another timescale of interest is the timescale over which wind ram pressure in the initial clump frame $P_{ram} = \rho_1 v_1^2$ would accelerate the clump such that the bow shock would dissipate, τ_{ram}. The relevant equations for this are the following

$$\begin{aligned} P_{ram} A &= m_c \frac{dv_c}{dt} \\ \rho_1 (v_1 - v_c)^2 A &= \rho_2 A l_c \frac{dv_c}{dt} \end{aligned} \tag{3.2}$$

Where v_c is the clump velocity in relation to its original frame of rest, A is the cross sectional area presented to the wind, and the mass of the clump, m_c, is assumed to be $\rho_2 A l_c$. We can solve this differential equation as follows, assuming the bow shock will dissipate when $v_1 - v_c = c_s$.

$$\begin{aligned} \int_0^{v_1 - c_s} \frac{1}{(v_1 - v_c)^2} dv_c &= \frac{\rho_1}{\rho_2 l_c} \int_0^{\tau_{ram}} dt \\ \tau_{ram} = \chi_B l_c (\frac{1}{c_s} - \frac{1}{v_1}) = \frac{M_B^2 l_c}{v_1}(M_B - 1) &= \frac{M_B l_c}{c_s}(M_B - 1) \\ \frac{\tau_{ram}}{\tau_{cc}} &= \frac{M_B^2}{\sqrt{\chi_c}}(M_B - 1) \end{aligned} \tag{3.3}$$

For large bow shock Mach numbers eq. 3.3 reduces to $\tau_{ram}/\tau_{cc} = M_B^3/\sqrt{\chi_c}$. Thus only low Mach number clumps are actually accelerated back up to the wind speed in the simulation time presented here. Since the clumps are dense and slow with respect to the wind they produce a low density cavity behind the clump as the wind deflects around them. The extent of the cavity is simply $l_{cav} = v_1 t_{clump} = M_B c_s R_c/(v_w - M_B c_s)$, where t_{clump} is the how long the clump has been in the wind for and R_c is the radial distance between the start location of the clump and its current location.

3.2.3 Cosmic Ray Evolution

Figure 3.6 shows the CR proton spatial distribution in terms of $p^4 f$ at the injection momentum ($p_{inj} = 0.01$) for $t = 0.75$. As noted in §3.2.1 due to the high magnetic field in the clump the CRs are confined to the shocked clump region, particularly at low momenta. The enhanced magnetic field in the clump scales as M_B^2 which leads to a magnetic field increase of 1-2 orders of magnitude. This reduces the diffusion length by the same factor, effectively confining low momenta CR's to the shocked region.

However, as the momentum of the CRs increases they are able to leak out of the shocked clump, as demonstrated in Figure 3.7 which shows the proton spatial distribution at $p = 1$. The characteristic momentum at which the CRs leak out of the clump will be when the diffusion length of the CRs in the clump equals the clump size, $l_c = \kappa/v_2$. Putting in the relations that are derived in §3.2.2 we arrive at $l_c = \kappa_o p/(B_1 \chi_B v_2) = \kappa_o p/(B_1 M_B c_s)$. Thus the characteristic momentum will be $p = B_1 M_B c_s l_c/\kappa_o = 0.03(B/1\text{ mG})M_B(l_c/R_s)$. Thus in Figure 3.7 at $p = 1$ the majority of shocks will no longer confine the protons and therefore there are no large concentrations of CRs at the shocks as there was in Figure 3.6.

The region behind the clump is a low density, low magnetic field zone as noted in §3.2.2 and see in Fig. 3.3. When the CRs that escape the clump diffuse into this region their diffusion length increases correspondingly. The increase in diffusion length allows the CRs to fill the void in a short amount of time. While this effect is not prominent in the protons, it is for the electrons at high momenta that are subject to energy losses. Figure 3.8 shows the electron spatial distribution at $p = 0.1$. In Figure 3.8 one can see large tails of electrons behind the clumps. These tails are created by the electrons filling the cavity the exists behind the clump before suffering significant energy losses. Whereas, outside the cavity the electrons do not diffuse far before succumbing to energy losses. As the IC lifetime at high momentum is very short, this implies that the diffusion length in the cavity region is large. The long diffusion length shows that the magnetic field is weak in the cavities, which is expected due to magnetic field mimicking the gas density as discussed in the previous section.

The volume integrated spectrum for the CR protons and electrons, $p^4 F = \int p^4 f(p) dV$, excluding the thermal population is shown in Fig. 3.9. Both the proton and electron spectrum have a spectral slope of approximately 4, characteristic of acceleration at

strong shocks. As noted in §3.2.2 for isothermal shocks a compression ratio of 4 is reached very quickly at a Mach number of 2. Thus virtually all the shocks on the grid will have compression ratios greater than their adiabatic analogs. The CR acceleration is primarily dependant on the divergence of the velocity across the shock. As such the CRs in the isothermal case will see every shock as a strong shock and will take on a powerlaw slope of 4 indicative of that fact.

The high energy cutoff of the proton spectrum is around $p = 1$ (E = 1 GeV). This is due to the protons no longer being confined by the clumps, as noted earlier in this section. CR's of this energy are able to stream freely away from the clump. However the highest energy accelerated at the shocks is not expected to be uniform with radius. Since the magnetic field scales as $1/R$, we would expect the proton highest energy protons accelerated to scale likewise as the confinement at the shock is controlled by the magnetic field.

For the electrons the high energy cutoff is around $p = 0.05 - 0.1$ (E = $50 - 100$ MeV). The electron cutoff energy is controlled by two competing processes, energy gain of the electrons at the shock and energy loss due to IC energy losses. To find this energy one can equate the shock acceleration timescale, τ_a, and the energy loss timescale, τ_r. The relevant equations for each of these processes are (Blumenthal & Gould 1970; Blandford & Eichler 1987)

$$\tau_a = \frac{\kappa}{u_s^2} = 313 \text{ sec } p \left(\frac{1 \text{ G}}{B_s}\right) \left(\frac{100 \text{ km/s}}{u_s}\right)^2 \left(\frac{v_w}{v_{rot}}\right) \left(\frac{R}{R_s}\right)$$

$$\tau_r = \frac{3}{4} \left(\frac{m_e}{m_p}\right)^2 \frac{m_p c}{\sigma_T} \frac{1}{u_r} \frac{1}{p} = 2.47 \text{ sec } \frac{1}{p} \left(\frac{R}{R_s}\right)^2 \left(\frac{L_s}{L}\right)$$

$$E_{e,peak} = p_{e,peak} m_p c^2 = 14 \text{ MeV} M_B \left(\frac{T}{T_w}\right) \sqrt{\left(\frac{B_s}{1 \text{ G}}\right) \left(\frac{v_{rot}}{v_w}\right) \left(\frac{L_s}{L}\right) \left(\frac{R}{R_s}\right)} \quad (3.4)$$

The above formula shows that the maximum electron energy should scale as $R^{1/2}$.

The radial evolution of the protons and electrons can be seen in Figure 3.10, where $p^4 F$ is calculated for annular bins centered on the star with a radial width of $25 R_s$. The proton distribution starts off flatter in the interior of the wind then develops a slight slope further out in the wind. The annuli at larger radii contain more particles as expected as they contain more volume. However the largest radii shows a drop which is

due to the clumps not completely filling that region. For the most part the distributions are generally the same and show no sign of the $1/R$ evolution that we would expect for the highest energy protons. However the protons do not lose energy except due to adiabatic expansion which is not significant over such short timescales. As such the protons accelerated to high energy when the clump was closer to the star will remain close to that energy and will fill in the higher energy bins even if there is no further particles being accelerated up to that energy. Thus the high energy cutoff will not change significantly until much larger radii.

The electrons show a similar evolution radially to the protons, except for the high energy cutoff which declines with radius. This is contrary to our expectation of a scaling of $R^{1/2}$. Implicit in that discussion was the assumption that the electrons were confined to the shock and thus continually accelerated. However, at larger radii the confinement momentum becomes smaller than the momentum calculated in Eq. 3.4 which ruins the derived scaling relation. Thus the peak momentum accelerated by the electrons is controlled by balancing the acceleration time, energy loss time, and the confinement of the electrons to the shock.

3.3 Summary

We preformed a multidimensional MHD-DSA simulation of wind-embedded shocks near an O-star assuming an isothermal wind. This simulation tracked the evolution of both proton and electron populations including appropriate energy losses. The wind-embedded shocks were seeded from the results of previous line driven instability calculations. The instabilities develop into dense clumps that propagate slower than the wind.

Unfortunately, the combined effects of the isothermal nature of the wind and a diffusion coefficient dependant on the local magnetic field precluded any inclusion of CR feedback in the dynamics. This was due to the intense magnetic field at the shocks confining the majority of the particles to a very small region, thereby restricting the ability of the CR pressure to weaken the shock. This creates a dense region of high CR pressure which led to numerical instability. A further more dedicated study of CR modified isothermal and radiative shocks is warranted in light of these results.

The bow shocks for the wind clumps are typically Mach 2-6. While not impressive by adiabatic terms, in an isothermal setting this shock velocity is enough to create compression ratios by of 4-36. Thus virtually every shock in the wind is strong, at least in the adiabatic sense of the term.

The CR spectrum for both electrons and protons has a spectral index of approximately 4, consistent with acceleration at strong shocks. The maximum electron energy is about 100 MeV, which is controlled by the balance between shock acceleration and energy losses due to IC. However at large radii, the confinement of the electrons to the shock becomes important as well. The maximum proton energy is around 1 GeV, which is controlled by the particle confinement by the magnetic field at the shock.

It is clear from these simulations that wind-embedded shocks can be efficient particle accelerators. Though the effects of CR feedback have not been included, it is evident that their contribution to the flow dynamics will be important. If the inclusion of CR feedback disrupts the high compression ratio of the shocks, then they will cease to be efficient accelerators as the CRs will no longer be effectively confined to the shock by the magnetic field. In light of these results let us move forward and investigate CR acceleration in the colliding wind binary scenario.

Parameter	Value
M_s	22 $M_\odot$
R_s	8.5 $R_\odot$
L_s	2.3×10^5 $L_\odot$
$B(R_s)$	10 G
R_{in}	50 R_s
R_{out}	200 R_s
v_w	2000 km/s
$\dot{M}$	10^{-6} $M_\odot$/yr
v_{rot}	25 km/s
T_w	10^4 K

Table 3.1: Wind Instability Model Parameters

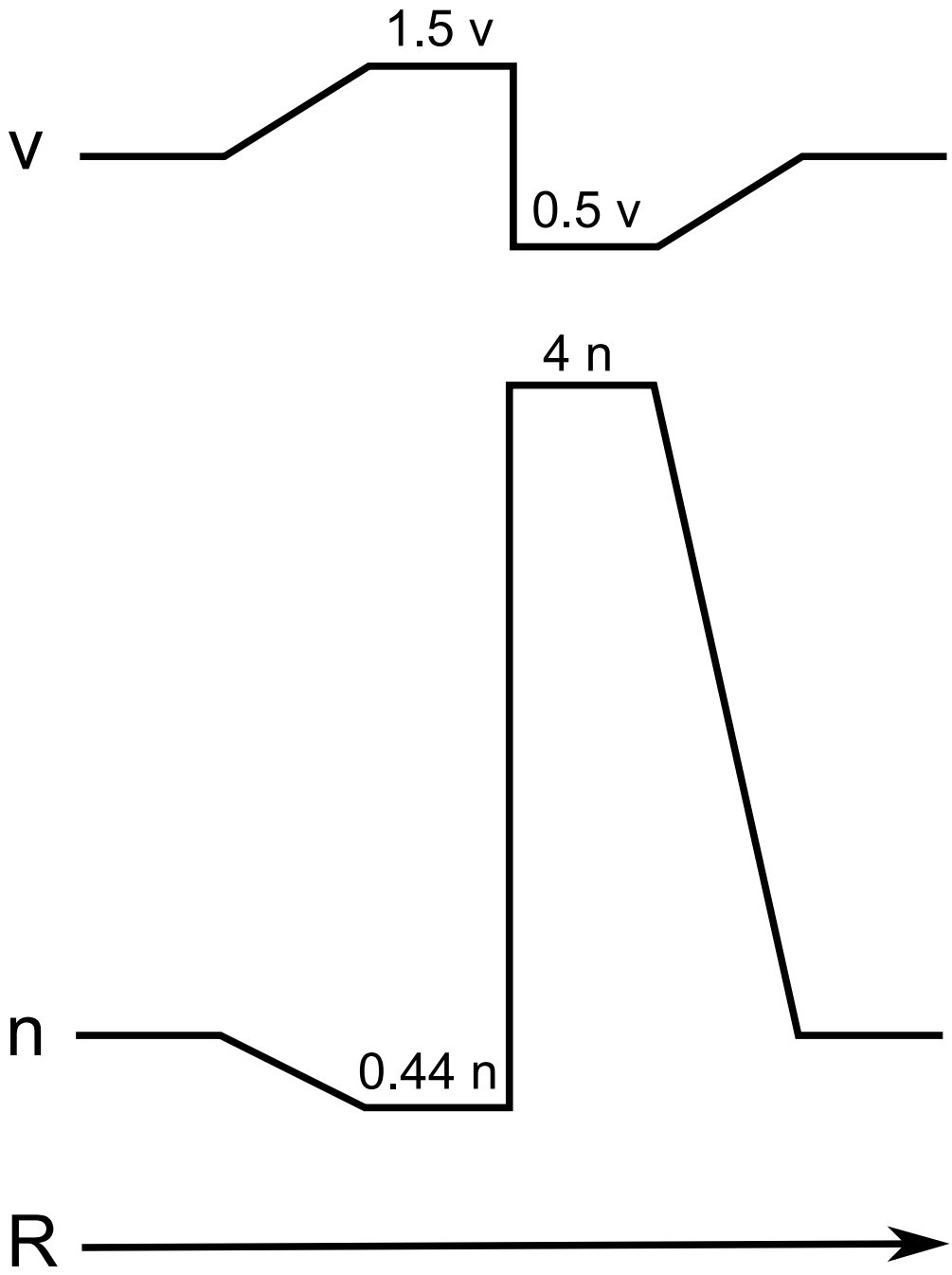

Figure 3.1: Illustration of the maximum line driving instability model used.

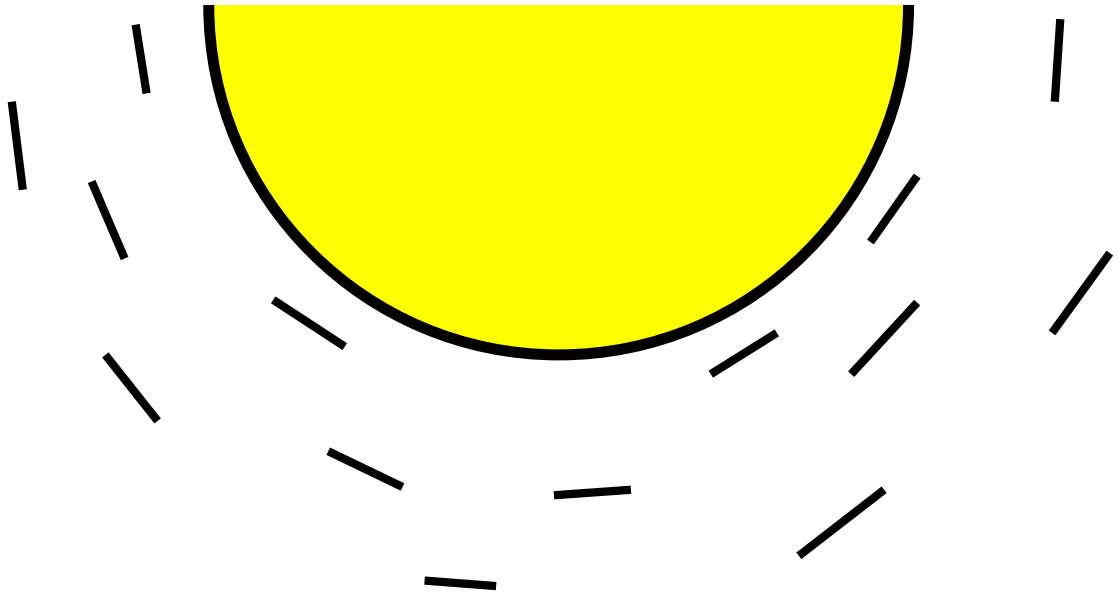

Figure 3.2: Illustration of instability placement around driving region.

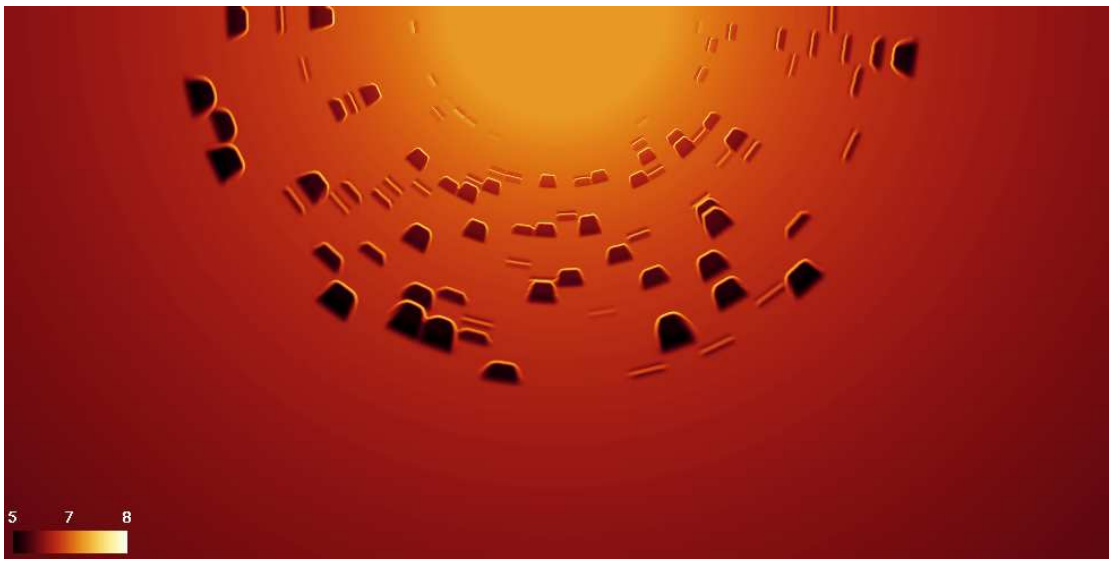

Figure 3.3: Logarithm of the Gas Number Density at $t = 0.75$.

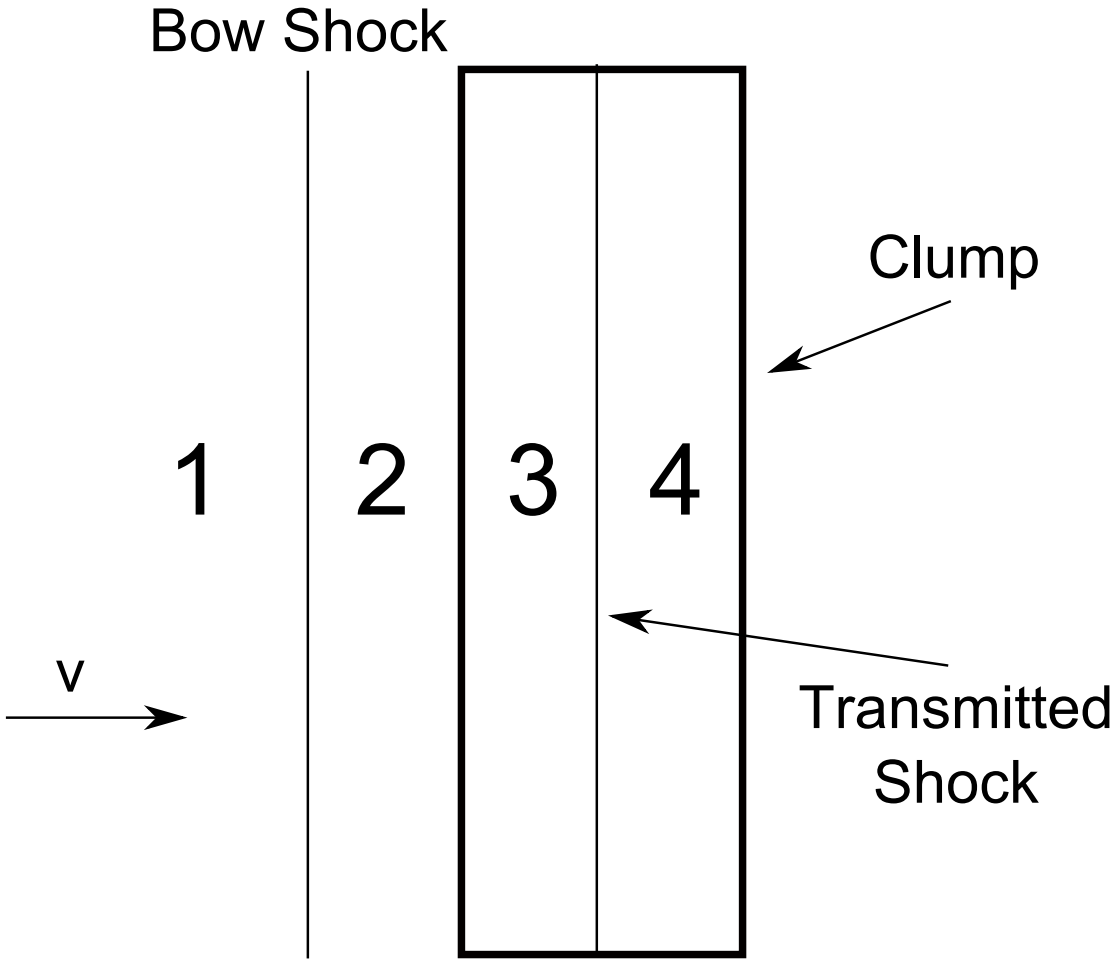

Figure 3.4: Illustration of clump. Region 1 is the upstream flow, region 2 is the post bow shock flow, region 3 is the shocked clump, and region 4 is the unshocked clump.

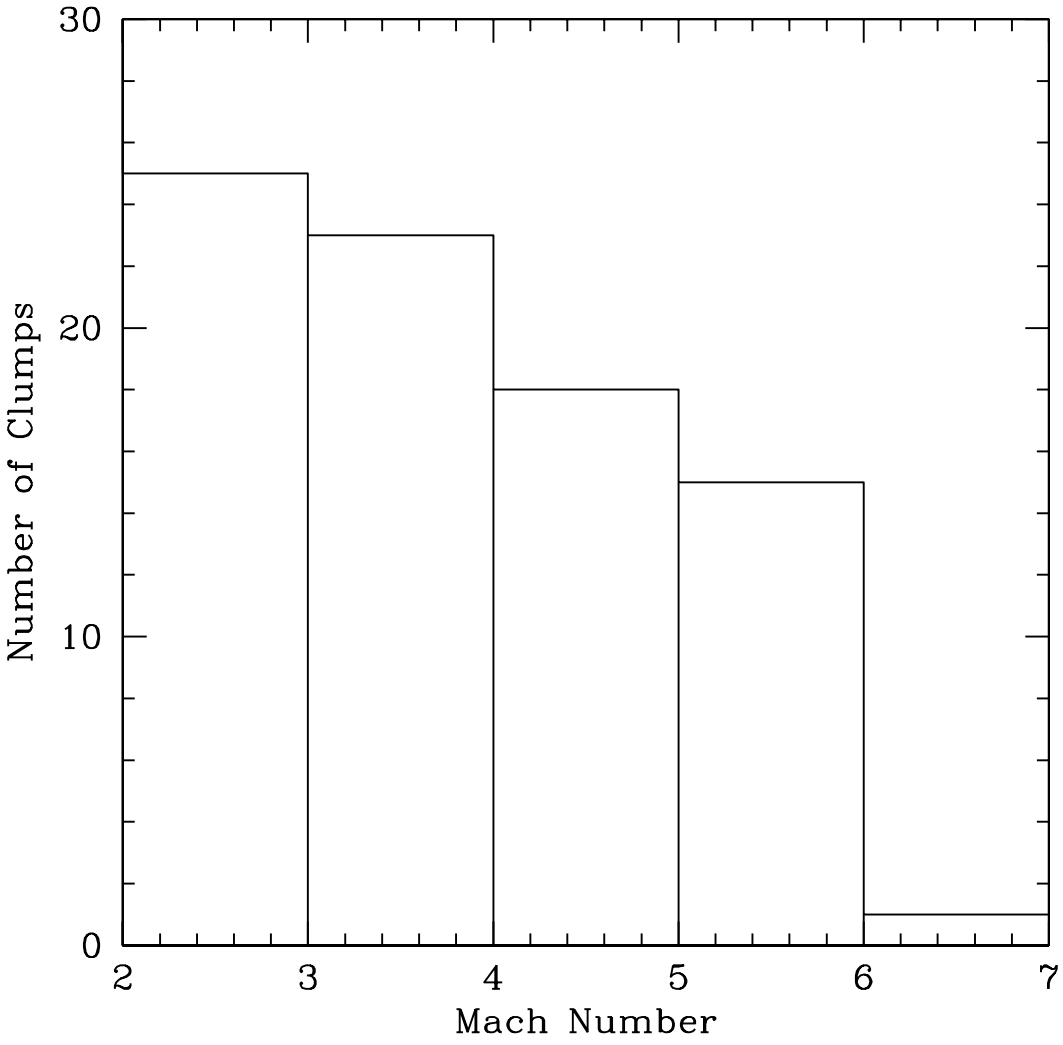

Figure 3.5: Histogram of Number of Clumps at particular Mach Numbers at $t = 0.75$.

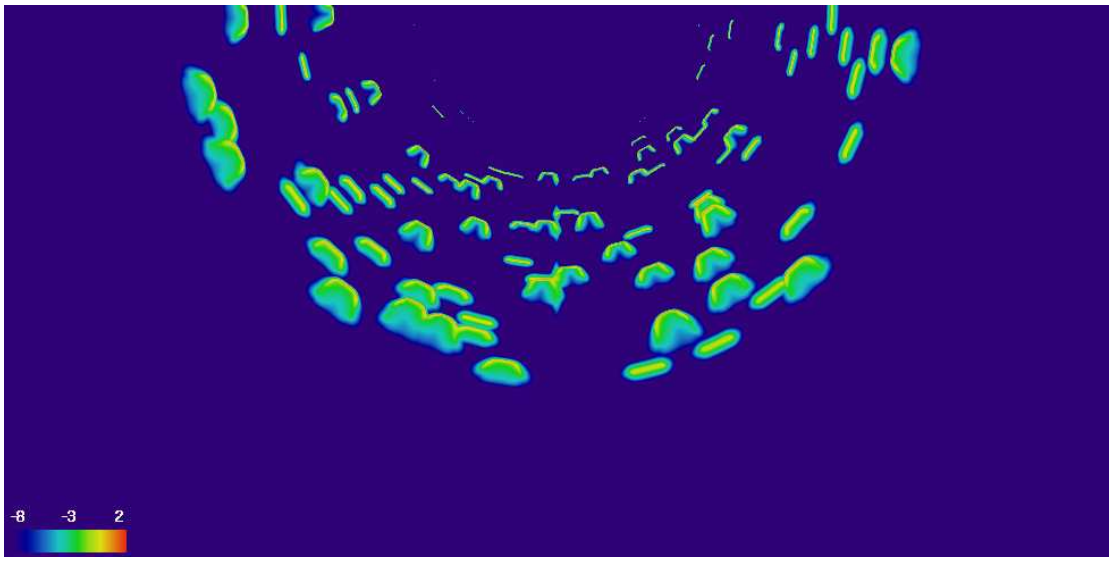

Figure 3.6: Logarithm of $p^4 f$ for protons at the injection momentum of $p = 0.01$ at $t = 0.75$.

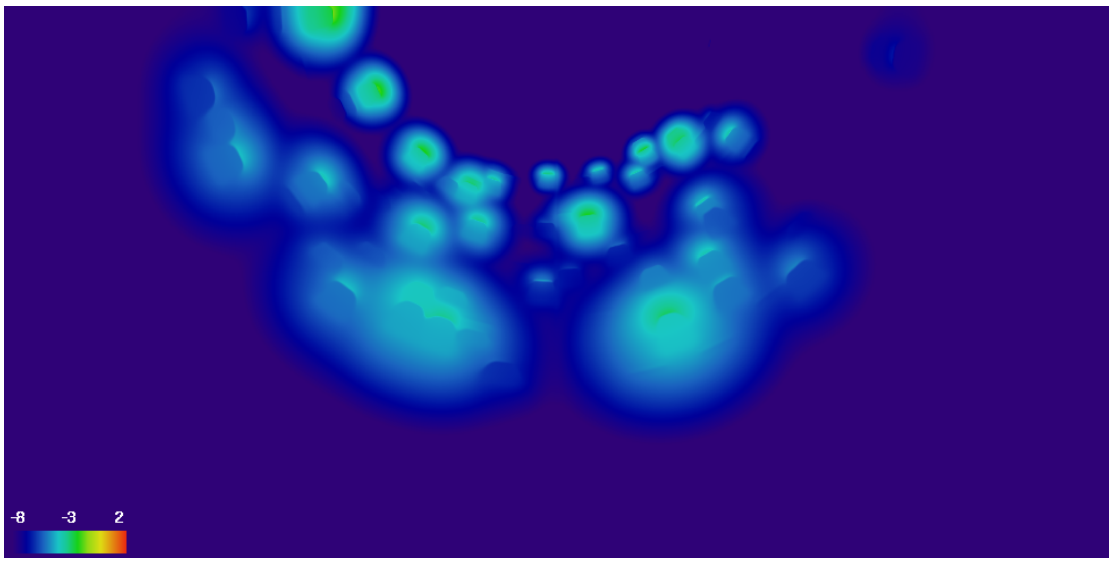

Figure 3.7: Logarithm of $p^4 f$ for protons at $p = 1$ at $t = 0.75$.

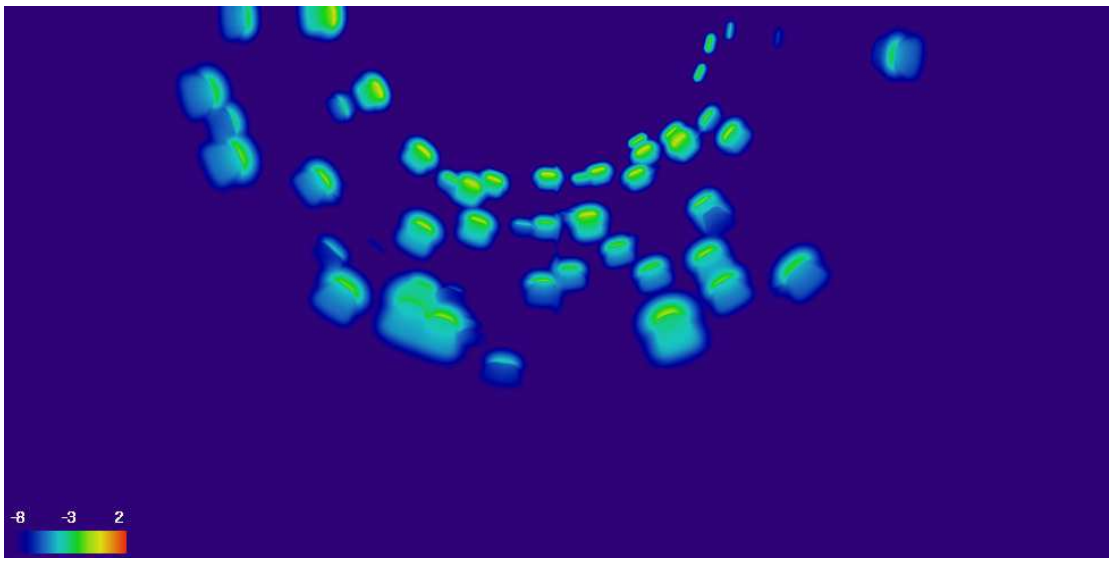

Figure 3.8: Logarithm of $p^4 f$ for electrons at $p = 0.1$ at $t = 0.75$.

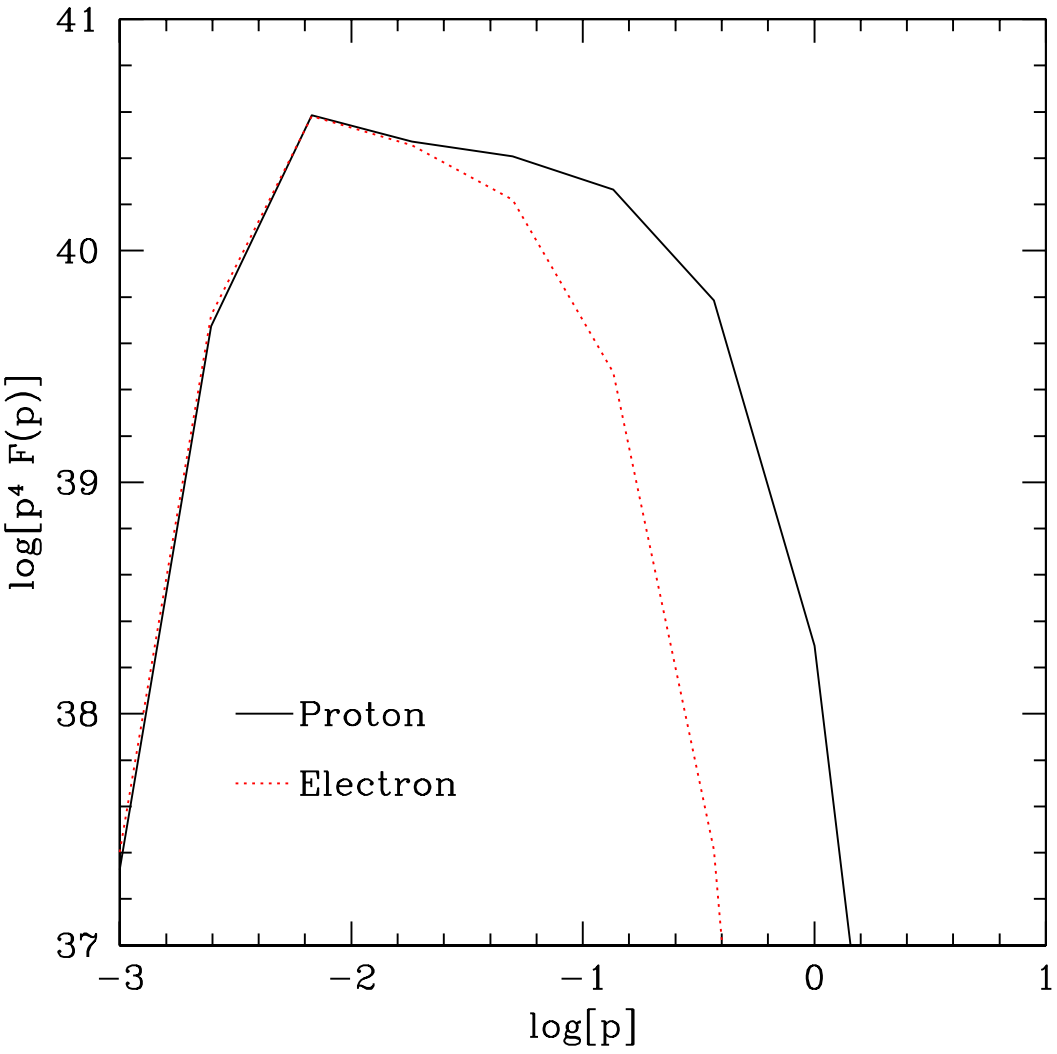

Figure 3.9: Integrated CR spectra for protons and electrons at $t = 0.75$.

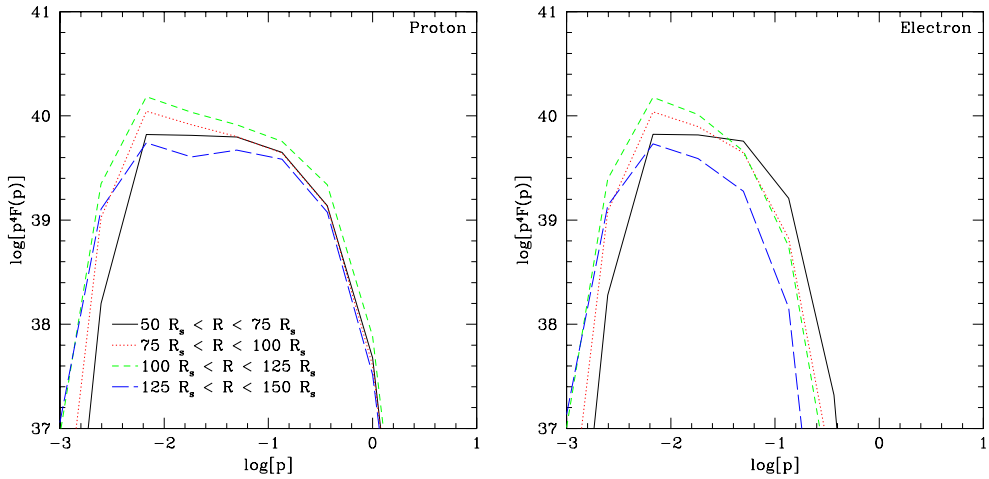

Figure 3.10: Integrated CR spectra in Annular Bins at $t = 0.75$. Protons on the left, electrons on the right.

Chapter 4

Multidimensional DSA in a O+O star Colliding Wind Binary

As noted in the Chapter 1, the colliding wind binary scenario is the favored scenario to explain the nonthermal emission seen from O-stars. Thus understanding the effects of CR acceleration on the CR spectrum and MHD of the system is very important to understanding the radiative emissions. Similar to the previous chapter we will first lay out our simulation set up in §4.1 and then in §4.2 we will discuss the results of the simulation.

4.1 Numerical Method

Similar to Chapter 3 we again neglect gravity, radiative driving, as well as radiative heating and cooling for this simulation. Thus we will only treat the MHD-DSA for this simulation. We will discuss the particulars of MHD-DSA solver used for this simulation in §4.1.1 and in §4.1.2 we layout the initial conditions for this simulation.

4.1.1 MHD-DSA Solver

We will use the DSA solver describe in Chapter 2 in conjunction with the WOMBAT MHD solver combined with the injection model described in the next section which replaces the one discussed in Chapter 2. As we did in Chapter 3 we will use 2.5-D

cylindrical coordinates to simplify the simulation and reduce computational cost.

4.1.1.1 Injection

Injection for this model is handled via a simple flux fraction model which is injected as a spectrum over multiple bins rather than into a single momentum bin. In this model a small, fixed fraction of the thermal particle flux through the gas subshock, ϵ_{inj}, is injected as a powerlaw spectrum at the subshock. As in the previous injection model, the minimum momentum for the powerlaw spectrum is $p_{min} = \alpha c_{s_2}$, where α is a constant greater than unity and c_{s_2} is the plasma sound speed immediately downstream of the subshock (e.g. Jones & Kang (2005)). We will set $\alpha = 2.0$ for this simulation, which is the commonly accepted value (Jones & Kang 2005). The maximum momentum, p_{max}, for the powerlaw spectrum is the momentum at which the particle's precursor diffusion length becomes computationally resolved which occurs when $\kappa(p_{max})/u_s > 10\Delta x$ (Jones & Kang 2005). The spectral slope is determined from the standard formula for test particle DSA, $q = 3\chi/(\chi - 1)$, where $\chi = \rho_2/\rho_1$ which is the subshock compression ratio (Blandford & Eichler 1987).

This gives a source term for equation 2.1 of $S(p) = \epsilon_{inj}(\rho_1/(\mu mp))u_s w(x - x_s)(q - 3)/(p_{min}^{3-q} - p_{max}^{3-q})p^{-q}$. Where μ is the mean molecular weight, u_s is the subshock speed with respect to the plasma immediately upstream, x_s is the location of the shock center, and w is a normalized weight function that allows the injection to be distributed across the numerical shock structure. This distribution is put in place in order to prevent discontinuities in the CR distribution. The energy extracted from the thermal plasma is simply $L = \frac{1}{2}\epsilon_{inj} w(x)\alpha^2 c_{s_2}^2 \rho_1 u_s$.

The above model for injection assumes that the spectrum below p_{max} can be expressed in a form appropriate for test particle DSA. This implicitly assumes that any shock modification occurs over larger scales than the characteristic precursor diffusion length of p_{max}. Previous simulations of CR modified shocks with Mach numbers greater than 10 have demonstrated that for energies below around 1 GeV the CR spectrum can be expressed in test particle form (Kang et al. 2009). The shocks in this simulation have Mach numbers much greater than 10. As such this assumption should be valid so long as the injected spectrum is tied to the evolution of the subshock structure.

4.1.2 Simulation Setup

The initial conditions used for the winds from the stars in this simulation are almost identical to the winds described in §3.1.2. This is to aid in comparing the results of the two simulations against one another in Chapter 5. The nature of the stars, stellar wind velocity, mass loss rate, magnetic fields, particle diffusion, and particle energy losses are all the same as in §3.1.2. As such we will only describe the components that are different in this simulation from the previous one. Table 4.1 contains the parameters for the simulation.

In this simulation we no longer inject line driven instabilities into the wind, nor do we use the isothermal assumption. We also assume that both stars are identical and have identical winds. This is done in order to simplify the simulation. For electron energy losses due to IC, the radiation field now includes the effects from both stars.

As in Chapter 3, the wind temperature is maintained at 10^4 K due to photo-ionization from the star's ultraviolet (UV) flux which prevents the wind from cooling due to adiabatic expansion (Lamers & Cassinelli 1999). The wind is not only heated due to the radiation flux from the star but strong metal lines cool the gas when heated above 10^4 K (Kholtygin et al. 2003). The shocks generated by the colliding winds have a very high Mach number ($M_{sh} = 120$) and heat the ambient wind to $\sim 5 \times 10^7$ K. This temperature is too hot for efficient metal line cooling. As such the cooling length is much larger than the simulation domain. This is in contrast to Chapter 3, where the cooling length was much shorter than the simulation resolution. To effectively model this situation we will treat the wind as an adiabatic fully ionized proton-electron plasma ($\gamma_g = 5/3$) with a temperature floor of 10^4 K. This will allow the shock to heat normally while preventing the wind from cooling below 10^4 K due to the expansion of the winds.

Similar to previous simulation, the wind driving region has a radius of 50 R_s, which is well outside of the wind acceleration zone. The separation, D, between the two stars is 400 R_s. This gives an orbital period for the two stars of 3.37 years and an orbital velocity of 11 km/s. This velocity is much less than the wind velocity and the orbital period is much longer than the dynamical time for the winds. Therefore we will ignore effects due to the orbital motion.

The expected maximum proton energy in this simulation can be found based on the condition that the characteristic precursor diffusion length, $l_d \sim \kappa/u_s$, of the particle

be contained in the system that is accelerating it. Using a characteristic magnetic field strength of 1 mG at the shocks, a shock velocity of 2000 km/s and a physical extent of 400 R_s we expect the maximum momentum for the CR protons to be about $p \approx 1000$ ($E \approx 1$ TeV). Knowing this we will set the CR momentum range to span 16 momentum bins logarithmically spaced between $0.000912 < p < 8106$.

Given the requirements for injection discussed in §4.1.1.1 we set our maximum injection momentum at $p_{max} = 0.368$ and the grid resolution to $\Delta x = 0.03333$ R_s. The total box size extends from -300 R_s < z < 300 R_s and $0 < r < 100$ R_s with the stars located at ± 200 R_s giving a total box size of 18000×3000. Thus the simulation region is focused on the apex of the colliding wind flow. This is the region where most the most efficient acceleration is expected to take place. The higher efficiency is due to the higher shock Mach numbers and high magnetic fields in this region due to the proximity to the stars. Since we care about the MHD-DSA evolution when the colliding wind systems reaches steady state, we initially run a pure MHD simulation to get the system in to its steady state configuration. Once steady state is achieved, we then turn on the DSA portion of the code and allow the CRs to affect the shock evolution from then on out.

4.2 Results

4.2.1 MHD Evolution

The top panel of Figure 4.1 shows the gas number density when the pure MHD simulation reaches steady state. In steady state without CR feedback the colliding winds form into two standing reverse shocks ($M_{sh} = 120$). A contact discontinuity separates the flows from each stars. Since the stars are the same in terms of flow parameters the contact discontinuity is located at $D/2$. To measure the importance of the magnetic field we will use β, which is defined as the ratio of the gas pressure to the magnetic pressure. In this simulation $\beta = 300$. As such we can safely ignore the magnetic field in terms of its effects on the dynamics. The large β also means that the azimuthal magnetic field is frozen into the plasma and mimics the evolution of the density.

The expected position of the two shocks in steady state can be derived as follows assuming the shock separation is much smaller than D (e.g., Luo et al. (1990)). Let us consider a cylinder that has its z axis aligned with the line that connects the two stars,

see Figure 4.2 for illustration. For this exercise we will constrain ourselves to the region around the apex where the shocks can be approximated as plane shocks. We will set the length of the cylinder along the z axis to be the distance between the two shocks, h. The radius of the top and bottom of the cylinder will be s.

In steady state the amount of material flowing into this cylinder must be the same as the amount flowing out. The net flux of material into the top and bottom of the cylinder is defined by the amount of material flowing into the shocks, which is simply $2A\rho_w v_w$. A is the surface area of the top or bottom of the cylinder, πs^2. The flux of material leaving the sides of the cylinder is defined by the conditions in the postshock medium. In the postshock environment the density of the wind is compressed by a factor $\chi_t = \rho_2/\rho_0$. As discussed in §2.1, '2' is the postshock conditions and '0' is the unmodified, upstream conditions. The velocity in the direction of the shock normal stagnates as the opposing velocities of the flows from the two stars cancel the wind's momentum in this direction. This cancellation means the velocity parallel to the shock does not contribute to the flux out of the cylinder. Since the stellar winds flow out radially from the stars and the shocks are planes there is also a velocity component that is perpendicular to the shock normal. This component is not affected by the shock or the opposing wind and can be approximated as $v_\perp = 2v_w s/D$. Combining the postshock density with this velocity we end up with a mass flux of $2W\chi_t\rho_w v_w s/D$. W is the surface area of the side of the cylinder, $2\pi sh$. Setting the flux into the cylinder equal to the flux out and doing some algebra we end up with the condition that $h = D/(2\chi_t)$. Thus for a strong shock $h = D/8$ which corresponds nicely with the shock separation seen in Figure 4.1.

The bottom panel of Figure 4.1 shows the gas number density when the combined MHD-DSA reaches steady state. The total compression ratio of the gas, χ_t, has increased to a factor of about 4.5. The higher compression is typical of CR modified shocks as the precursor compresses and heats the gas before it encounters the subshock. The heating while enough to give a boost to the density flowing into the subshock is not enough to weaken the compression at the subshock which is still a factor of 4. The additional compression effects the distance between the two shocks such that now their separation is $D/9$, a net change of about 10%

An image of the CR pressure normalized by a characteristic wind ram pressure can be seen in Figure 4.3 in steady state. The characteristic undisturbed wind ram pressure

used is $\rho_{w,R_s}/(D/2)^2 v_w^2$. Where ρ_{w,R_s} is the density of the wind at the stellar surface. This is the ram pressure at the contact discontinuity if the wind was unshocked. It is approximately the same ram pressure seen by the shocks since $D \gg h$. One can see that the CR pressure is mainly confined to the immediate upstream region of the shocks and the postshock region. In the postshock flow about 15% of the incoming ram pressure is converted into CR pressure. This causes a corresponding drop in the gas pressure. When combined with the increase in density the resulting postshock temperature is lower than it would normally be for a shock of this Mach number. However this temperature change is not enough to move the postshock medium into a regime where it would strongly cool due to line emission.

If the injection of CR's were stronger than what is modeled here we expect there to be significantly more shock modification. Based on the effects seen here we would expect the postshock density to increase and a corresponding decrease in the shock separation. We would also expect more preheating in the wind. However any heating of the wind by the CR precursor will take the wind away from its floor temperature of 10^4 K. This will make it susceptible to radiative line cooling. The same can be said for the postshock flow as the CR pressure typically weakens the shock Mach number. This can reduce the postshock temperature to a regime where cooling is important. The combined effects of radiative line cooling and CR feedback are not well studied as currently only two fluid models exist (e.g., Wagner et al. (2006)). As such further study in to the high CR injection regime and the effects of radiative line cooling is warranted.

4.2.2 CR Evolution

The volume integrated spectrum for the CR protons and electrons, $p^4F = \int p^4 f(p) dV$, excluding the thermal population is shown in Fig. 4.4. The spectral index of the proton and electron spectra is 4 at low momenta, indicative of strong shocks. Normally for CR modified shocks we would expect to see a curved spectrum. This curved spectrum is due to the differing velocity divergences seen by CR's of differing momenta. However, in this case the subshock compression is always 4 because the subshock is never modified to the point were it ceases to be a strong shock. This keeps the CR spectrum flat.

In §4.1.2 we stated that the peak proton momentum is $p_{max} = D u_s B/(2\kappa_o) \approx 1000$ ($E \approx 1$ TeV) which is consistent with Figure 4.4. This constraint comes from the

requirement that a particle must be confined by the system accelerating it. At larger diffusion lengths that D the particles see a diverging flow rather than a converging flow. At that point the particles will simply escape the system.

This can be seen by looking at the top panel of Figure 4.5 which shows the phase space distribution of $p^4 f$ for protons in a spatial cut that is parallel to the shock normal. Also around that same momenta the CRs are diffusing far enough to encounter both shocks. This is due to the postshock magnetic field being enhanced by a factor of roughly 4, which decreases the diffusion length correspondingly. Thus when the diffusion length inside the shocks equals the distance between the shocks, $D/9$, the CRs upstream of the shocks diffuse roughly the distance to the stars. This means that the effects of acceleration at both of the shocks is mitigated due to particles no longer being bound to the system.

For the electrons there is a spectral break at 100 MeV and then a high energy cutoff around 1 GeV. The spectral break at 100 MeV can be explained by the electrons cooling as they propagate away from the shock due to diffusion and advection. This effect can be seen clearly in the bottom panel of Figure 4.5 which shows the electron phase space distribution of $p^4 f$ in a spatial cut that is parallel to the shock normal. The regions close to the shock are dominated by the combined effects of particle acceleration and energy loss. As the particles move further from the shock they are no longer participating in the acceleration and only lose energy due to IC. At high energy only those regions close to the shock are contributing to the integrated spectrum. Whereas at lower energy the entire postshock region contributes to the integrated spectrum which is a much larger volume.

This behavior has been noted in the modeling supernova remnants as well (e.g., Berezhko et al. (2002)). In those studies it has been shown that the spectral break can be found by the following formula (Berezhko et al. 2002)

$$E_{e,break} = \frac{3m_e^2 c^3}{4\sigma_T u_r t} = 2.6 \times 10^{-2} \text{ MeV} \frac{L_s}{L} \left(\frac{R}{R_s}\right)^2 \frac{1 \text{ day}}{t} \tag{4.1}$$

where R is the distance to the shock, u_r is the radiation energy density, and t is the time it takes for the postshock flows to reach the contact discontinuity. In this simulation $R \sim 200 R_s$ and $t \sim 10$ days giving a break energy of 100 MeV. This spectral

break only shows up in the integrated spectrum as it created by a volume filling effect. At any given location in the postshock flow the CR spectrum will not show this break. Rather the spectrum is a simple powerlaw with a high energy cutoff dependant on the history of the electrons in that location.

The electron cutoff energy seen in Fig. 4.4 is determined by two competing processes, energy gain of the electrons at the shock and energy loss due to IC energy losses. To find this energy one can equate the shock acceleration timescale, τ_a, and the energy loss timescale, τ_r. The relevant equations for each of these processes are (Blumenthal & Gould 1970; Blandford & Eichler 1987)

$$\tau_a = \frac{\kappa}{u_s^2} = 3.13 \text{ sec } p \left(\frac{1 \text{ G}}{B_s}\right) \left(\frac{1000 \text{ km/s}}{u_s}\right)^2 \left(\frac{v_w}{v_{rot}}\right) \left(\frac{R}{R_s}\right)$$

$$\tau_r = \frac{3}{4} \left(\frac{m_e}{m_p}\right)^2 \frac{m_p c}{\sigma_T} \frac{1}{u_r} \frac{1}{p} = 2.47 \text{ sec } \frac{1}{p} \left(\frac{R}{R_s}\right)^2 \left(\frac{L_s}{L}\right)$$

$$E_{e,peak} = p_{e,peak} m_p c^2 = 833 \text{ MeV} \left(\frac{u_s}{1000 \text{ km/s}}\right) \sqrt{\left(\frac{B_s}{1 \text{ G}}\right) \left(\frac{v_{rot}}{v_w}\right) \left(\frac{L_s}{L}\right) \left(\frac{R}{R_s}\right)} \quad (4.2)$$

Assuming a shock location at about $D/2$ and shock velocity of 2000 km/s the expected peak electron energy is 8.3 GeV. This is close to the cutoff energy seen in Fig. 4.4 and is consistent with the peak electron energies seen in bottom panel of Figure 4.5.

4.3 Summary

We performed a multidimensional MHD-DSA simulation of O-star colliding wind shocks. This simulation tracked the evolution of both proton and electron populations including appropriate energy losses. It also included the effects of CR feedback.

With an injection fraction of 10^{-4}, about 15% of the wind ram pressure is converted into CR pressure at the shock. The resulting CR precursor is not enough to significantly reduce the flow velocity before it encounters the subshock. However, the compression in the precursor is enough to raise the total compression ratio, which in turn affects the shock separation. If a higher injection fraction where used the precursor heating and weakening of the subshock may be sufficient to put the flow in to a regime where radiative cooling is important. In this scenario the combined effects of strong CR feedback and

radiative cooling could dramatically change the dynamics.

The CR spectrum for both electrons and protons has a spectral index of 4, consistent with acceleration at strong shocks even though the shock is modified due to CR pressure. This is due to the heating by the CR precursor being weak. This in turn allows the subshock compression ratio to remain about 4. The maximum electron energy is about 1 GeV, which is controlled by the balance between shock acceleration and energy losses due to IC. The maximum proton energy is around 1 TeV, which is controlled by the particle confinement by the converging winds.

It is clear from these simulations that colliding shocks can be efficient particle accelerators and will be modified by CR pressure. With these results let us now take a larger look and compare with the results of the previous chapter.

Parameter	Value
M_s	22 $M_\odot$
R_s	8.5 $R_\odot$
L_s	2.3×10^5 $L_\odot$
$B(R_s)$	10 G
R_{in}	50 R_s
D	400 R_s
v_w	2000 km/s
$\dot{M}$	10^{-6} $M_\odot$/yr
v_{rot}	25 km/s
T	10^4 K

Table 4.1: Colliding Wind Binary Model Parameters

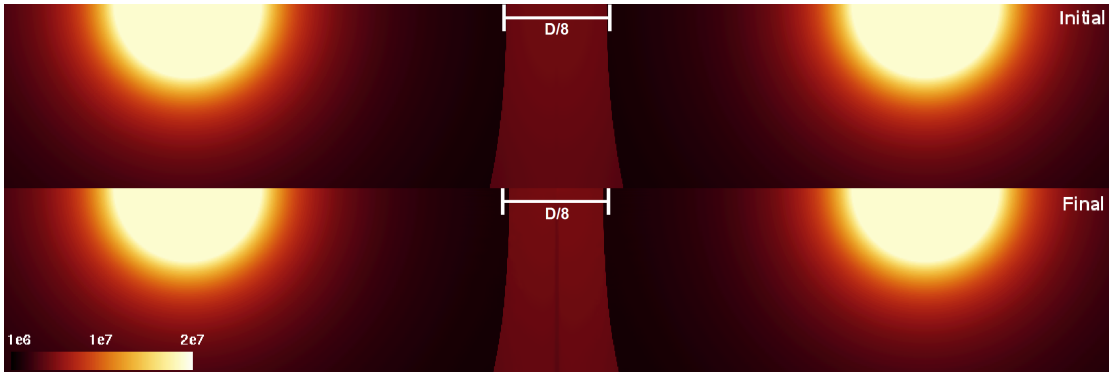

Figure 4.1: Image of the Density. Top image is from the initial conditions for when the DSA solver was turned on, the bottom is from the end of the simulation.

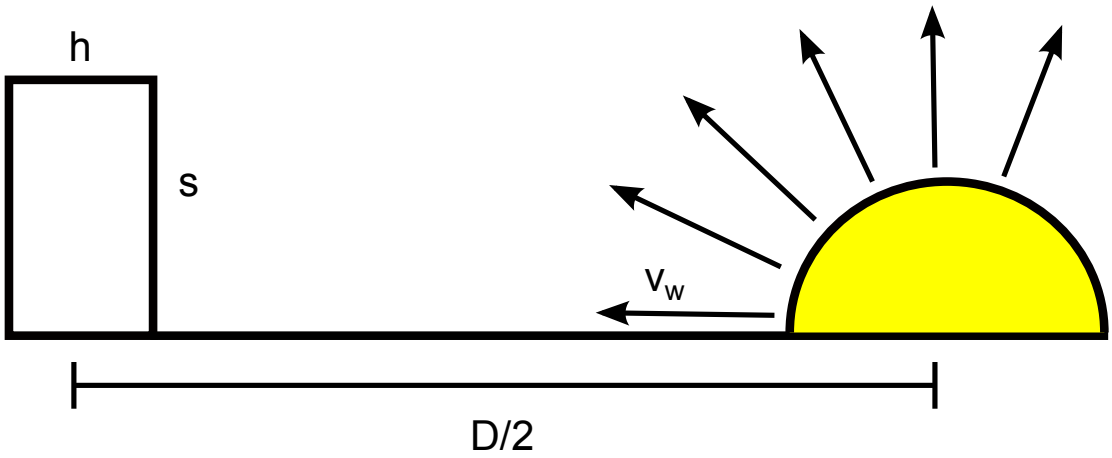

Figure 4.2: Schematic of cylinder used to derive the shock separation.

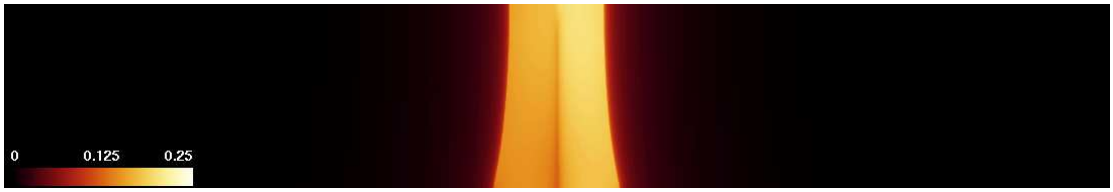

Figure 4.3: Image of the normalized CR pressure at the end of the simulation.

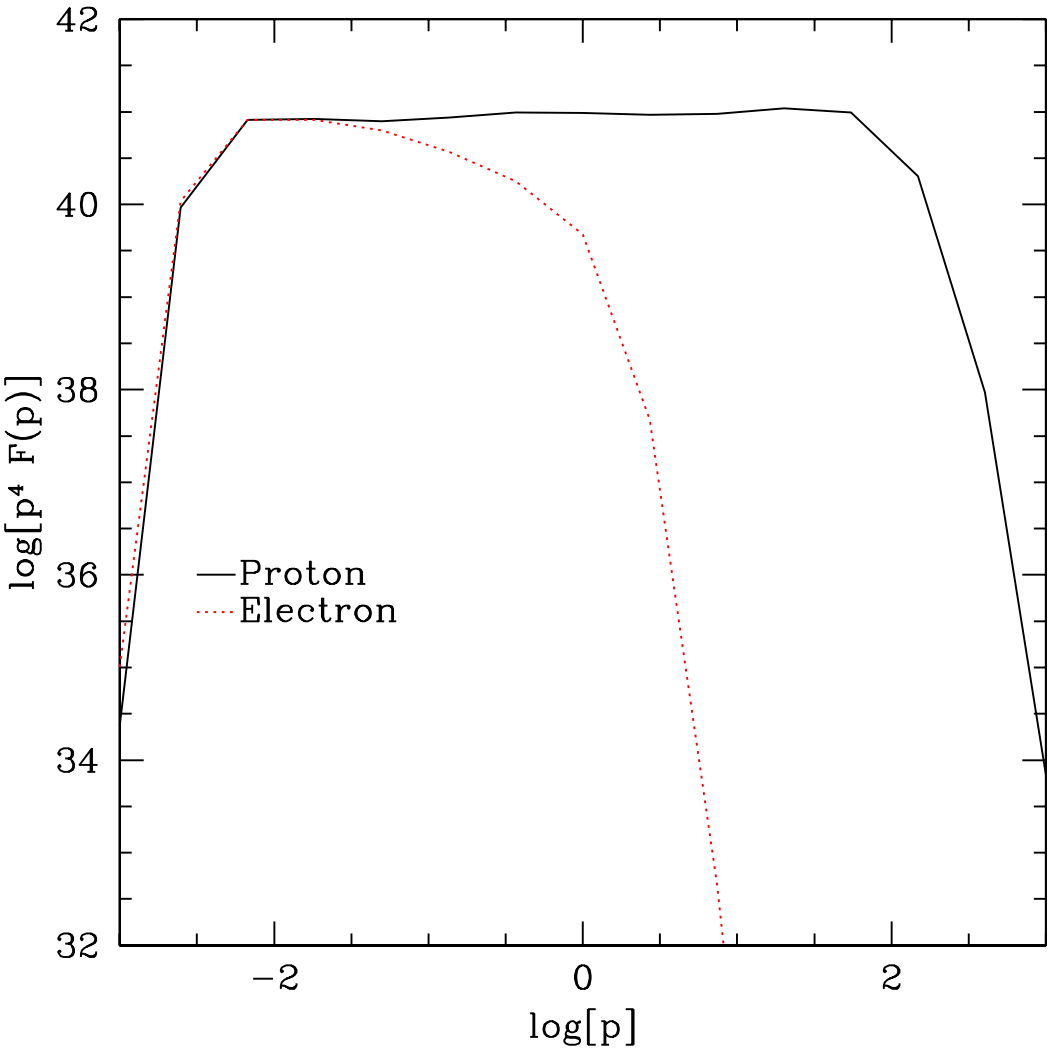

Figure 4.4: Integrated CR spectra for protons and electrons at the end of the simulation.

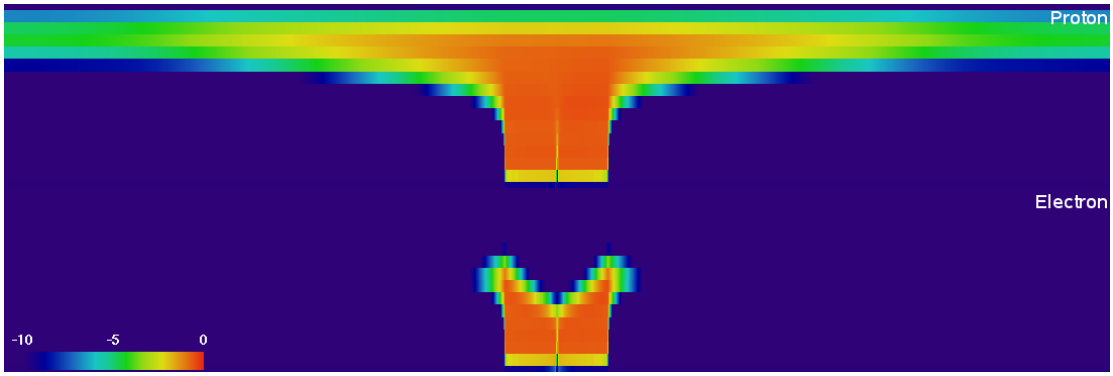

Figure 4.5: Phase Space of $p^4 f$ for a cut parallel to the simulation's z-axis in the middle of the grid. The horizontal axis of the image is location along the simulation's z-axis, and the vertical axis is in $ln(p)$. The top image is the protons and the bottom are the electrons.

Chapter 5

Conclusion and Discussion

5.1 Summary and Conclusions

We presented in Chapter 2 the first multidimensional DSA solver called MAST. This solver handles multidimensional CR acceleration self consistently using kinetic DSA. It was demonstrated that the MAST solver produces results approximately the same as normal kinetic solvers in one and two dimensions. This allows for the exploration of more complex multidimensional flows with the benefits of parallel computation and AMR.

With this new code we preformed two sets of multidimensional MHD-DSA simulations, one of wind-embedded shocks and the other of a colliding wind binary. In the following sections we will compare and contrast the two scenarios. First we will investigate the effects of CR feedback (§5.1.1). Next we will look at the CR spectra from both simulations (§5.1.2). We will then look at the potential for these two cases to explain the nonthermal emission (§5.1.3). Finally we will outline future work that needs to be done to understand these systems (§5.2)

5.1.1 CR Feedback

We modeled the wind-embedded shocks near an O-star as an isothermal wind, owing to the strong radiative heating and cooling in the wind. Unfortunately, the combined effects of the isothermal nature of the wind, and a diffusion coefficient dependant on the local magnetic field precluded any inclusion of CR feedback in the dynamics. Due to the

high compression ratios, the magnetic field was intensified at the shocks. The majority of the particles were confined by the field to a very small region. This restricted the ability of the CR pressure to weaken the shock. A dense region of high CR pressure was created which led to a numerical instability.

In the colliding wind case, CR feedback was successfully included. It was found that with an injection fraction of 10^{-4}, about 15% of the wind ram pressure was converted into CR pressure at the shock. The resulting CR precursor was not enough to significantly reduce the flow velocity before it encountered the subshock. However, the compression in the precursor was enough to raise the total compression ratio, which in turn affected the shock separation. If a higher injection fraction were used, the extra precursor heating and weakening of the subshock might have been sufficient to put the flow in to a regime where radiative cooling is important. In this scenario the combined effects of strong CR feedback and radiative cooling could dramatically change the dynamics.

Both these simulations illustrate the need for greater understanding of CR modified radiative shocks. As noted previously, very little research has been done into these type of shocks. This gap in our understanding needs to be rectified if we hope to understand more complex systems that include these effects. Thus more extensive 1-D modeling of DSA at radiative shocks in a simpler environment is needed.

5.1.2 CR Spectra

The CR spectra for both cases look very similar. Both have powerlaw slopes of approximately 4. In the wind embedded shock scenario this was due to the high compression at the shocks due to the isothermal nature of the wind. For the colliding wind case it was due to the subshock compression remaining 4 in spite of the CR precursor preheating the gas.

The maximum proton energies were determined by the diffusion lengths of the particles exceeding the scale of the systems accelerating them. This occurred at about 1 GeV for the wind embedded shock case and 1 TeV for the colliding wind binary. The maximum electron energy was controlled by the balance between shock acceleration and energy losses due to IC. However, for the wind embedded shocks particle confinement by the shock magnetic field becomes important at large radii as well. The maximum

electron energy was 100 MeV for the wind-embedded shocks, and 1 GeV for the colliding wind binary.

Both cases demonstrated efficient particle acceleration, though for different reasons. The isothermal conditions in the wind-embedded shock scenario gave rise to very high compression ratios. This made the shocks behave more like strong adiabatic shocks, even though the shock Mach numbers would be considered weak by adiabatic standards. In the colliding wind case, the shocks were strong and stationary allowing them to process significant amounts of CRs and accelerate them up to high energy.

5.1.3 Potential for Nonthermal Emission

Full analysis of the radiative emission from these simulations will not be covered in this work. We cannot safely provide an simple model for the spectral index of the emissions nor the magnitude. This is due to absorption processes and geometry playing a significant role in shaping the observed emissions (Reimer et al. 2006). However, we can estimate what energy bands these systems would be emitting in based on the peak particle energies.

For the electrons, synchrotron and IC will be the dominant nonthermal processes. At low frequency the synchrotron emission will be cut off due to free-free absorption and the local plasma frequency (e.g., Reimer et al. (2006); van Loo et al. (2006)). The synchrotron cutoff at high frequency is approximately the synchrotron critical frequency at the peak energy, $\frac{3}{2}\nu_B\gamma_{e,peak}^2$ (Blumenthal & Gould 1970). ν_B is the nonrelativistic cyclotron frequency and $\gamma_{e,peak}$ is the electron Lorentz factor at the peak energy.

In the case of the colliding wind binary assuming a characteristic magnetic field of 1 mG and a cutoff energy of 1 GeV, gives a frequency of about 20 GHz. For the wind-embedded shocks assuming a characteristic shock magnetic field of 20 mG and a cutoff energy of 100 MeV, gives a frequency of about 3 GHz. The actual peak frequencies would be higher if we had properly accounted for the Klein-Nishina limit in the electron energy losses. The magnetic field also varies considerably with location in the wind-embedded shock scenario, which could boost the peak frequency. Nonetheless, the synchrotron frequencies are in normal radio observation bands for these systems (e.g., van Loo et al. (2006)).

However, it is clear from these estimates that the colliding wind binary has more

potential to extend into high radio frequencies. This is important because free-free absorption becomes less important as the frequency increases. Thus the radio emission is less likely to be completely extincted due to absorption. On the other hand the wind-embedded scenario, with its lower peak frequency, could be quashed by the free-free absorption. While not conclusive until the full radiation modeling is done, it seems very likely that only the colliding wind binary scenario will be able to produce enough radio emission to exceed the absorption by the wind. This would exclude the wind-embedded shock scenario from being able to replicate the observed emission.

In IC the radiation spectrum for both systems starts in the soft X-ray then extend up to a peak electron energy of 1 GeV for the colliding wind, and 100 MeV for the wind embedded shocks. This is due to KN being an important effect in this environment. KN limits the peak energy of photons to be equal to the electron energy (Blumenthal & Gould 1970). With IC being produced throughout the X-ray band, these systems are fully capable of explaining the nonthermal X-ray measurements. However, the X-ray band is also dominated by thermal bremsstrahlung which can swamp out the IC signal.

For the protons, pion production via proton-proton collisions will be an important emission process in colliding wind binaries. The threshold for pion production is about 2 GeV, meaning that there is a considerable population of supra-threshold protons. The energy band for the pion spectrum can be found from the simple relation of $E_\gamma = 0.1E_p$ (Kelner et al. 2006). Thus the spectrum will extend from 200 MeV up to a peak photon energy of about 100 GeV. While not quite to TeV energies, the potential parameter space for these systems is large. Thus with more extreme parameters the colliding winds could produce TeV energy photons. In the wind embedded shock case, none of the protons are above the threshold energy. Hence, there will be no pion production.

5.2 Future Work

Full radiation models will be computed in the future for both simulations in order to compare them to the observations. These models will help investigate whether the wind embedded scenario is excluded or not. As noted before the effects of free-free absorption could completely extinguish the radio emission from the wind-embedded

shock scenario. The same question exists for the colliding wind binary, though with its emission extending to higher frequency it is less likely to be fully absorbed. It will also be of great interest to see if the resulting emissions from the colliding wind binary are analogous to the reported X-ray and gamma-ray observations.

However, caution must be taken with these future emission models as the combined effects of radiative cooling and CR feedback could significantly change the results from these simulations. To investigate this, new 1-D simulations will be undertaken to model DSA in radiative shocks. These new simulations will allow us to see how these shocks behave in the presence of CR feedback. The results from the simulations will lay the ground work for future DSA simulations of colliding wind binaries and wind-embedded shocks that include the effects of radiative line cooling in the shocks.

Future simulations will also model the outer wind collision region of the colliding wind binary scenario. This region contains the majority of the wind collision zone. Given the efficiency of the shocks in the colliding wind simulation, it is clear that the outer collision zone will be an important part of the CR acceleration picture in these systems. The large volume of this region could also contribute considerably to the radiative emission.

Bibliography

Aharonian, F., et al. 2007, A&A, 467, 1075

Benaglia, P. 2010, Astronomical Society of the Pacific Conference Series, 422, 111

Berezhko, E. G., Yelshin, V. K., & Ksenofontov, L. T. 1994, Astroparticle Physics, 2, 215

Berezhko, E. G., Ksenofontov, L. T., Völk, H. J. 2002, A&A, 395, 943

Bieging, J. H., Abbott, D. C., & Churchwell, E. B. 1989, ApJ, 340, 518

Blandford, R., & Eichler, D. 1987, Phys. Rep., 154, 1

Blomme, R. 2010, Astronomical Society of the Pacific Conference Series, 422, 178

Blumenthal, G. R., & Gould, R. J. 1970, Reviews of Modern Physics, 42, 237

Cappa, C. E., Arnal, E. M., Cichowolski, S., Goss, W. M., & Pineault, S. 2003, A Massive Star Odyssey: From Main Sequence to Supernova, 212, 596

Chen, W. 1992, Ph.D. Thesis

Chen, W., & White, R. L. 1994, Ap&SS, 221, 259

Choudhuri, A. R. 1998, The physics of fluids and plasmas : an introduction for astrophysicists / Arnab Rai Choudhuri. New York : Cambridge University Press, 1998. QB466.F58 C46 1998.

Chu, Y.-H. 2008, IAU Symposium, 250, 341

Cranmer, S. R., & Owocki, S. P. 1996, ApJ, 462, 469

Cunningham, A. J., Frank, A., Varnière, P., Mitran, S., & Jones, T. W. 2009, ApJS, 182, 519

De Becker, M., Rauw, G., Pittard, J. M., Antokhin, I. I., Stevens, I. R., Gosset, E., & Owocki, S. P. 2004, A&A, 416, 221

De Becker, M. 2007, A&A Rev., 14, 171

De Becker, M., Blomme, R., Micela, G., Pittard, J. M., Rauw, G., Romero, G. E., Sana,

H., & Stevens, I. R. 2009, American Institute of Physics Conference Series, 1126, 347

Donati, J.-F., & Landstreet, J. D. 2009, ARA&A, 47, 333

Dougherty, S. M., & Williams, P. M. 2000, MNRAS, 319, 1005

Drury, L. O., & Völk, J. H. 1981, ApJ, 248, 344

Drury, L. O. 1983, Reports on Progress in Physics, 46, 973

Dwarkadas, V. V. 2005, ApJ, 630, 892

Ellison, D. C., Moebius, E., & Paschmann, G. 1990, ApJ, 352, 376

Ellison, D. C., Giacalone, J., Burgess, D., & Schwartz, S. J. 1993, J. Geophys. Res., 98, 21085

Fullerton, A. W., Massa, D. L., & Prinja, R. K. 2006, ApJ, 637, 1025

Hamann, W.-R., Gräfener, G., Oskinova, L. M., & Feldmeier, A. 2009, American Institute of Physics Conference Series, 1171, 136

Jones, T. W., & Kang, H. 2005, Astroparticle Physics, 24, 75

Kang, H., Jones, T. W., LeVeque, R. J., & Shyue, K. M. 2001, ApJ, 550, 737

Kang, H., Jones, T. W., & Gieseler, U. D. J. 2002, ApJ, 579, 337

Kang, H., & Jones, T. W. 2006, Astroparticle Physics, 25, 246

Kang, H., & Jones, T. W. 2007, Astroparticle Physics, 28, 232

Kang, H., Ryu, D., & Jones, T. W. 2009, ApJ, 695, 1273

Kelner, S. R., Aharonian, F. A., & Bugayov, V. V. 2006, Phys. Rev. D, 74, 034018

Kholtygin, F. A., Brown, C. J., Cassinelli, P. J., Fabrika, N. S., Monin, N. D., & Surkov, E. A. 2003, Astronomical and Astrophysical Transactions, 22, 499

Kholtygin, A. F., Fabrika, S. N., Drake, N. A., Bychkov, V. D., Bychkova, L. V., Chountonov, G. A., Burlakova, T. E., & Valyavin, G. G. 2010, Astronomy Letters, 36, 370

Lamers, H. J. G. L. M., & Cassinelli, J. P. 1999, Introduction to Stellar Winds, by Henny J. G. L. M. Lamers and Joseph P. Cassinelli, pp. 452. ISBN 0521593980. Cambridge, UK: Cambridge University Press, June 1999.

Lee, H.-T., & Chen, W. P. 2009, ApJ, 694, 1423

Luo, D., McCray, R., & Mac Low, M.-M. 1990, ApJ, 362, 267

Mac Low, M.-M., McCray, R., & Norman, M. L. 1989, ApJ, 337, 141

Malkov, M. A., & O'C Drury, L. 2001, Reports on Progress in Physics, 64, 429

Marcowith, A., & Kirk, J. G. 1999, A&A, 347, 391

Owocki, S. 2009, American Institute of Physics Conference Series, 1171, 173

Panagia, N., & Felli, M. 1975, A&A, 39, 1

Pittard, J. M., & Dougherty, S. M. 2006, MNRAS, 372, 801

Pittard, J. M., Dougherty, S. M., Coker, R. F., O'Connor, E., & Bolingbroke, N. J. 2006, A&A, 446, 1001

Pittard, J. M. 2009, MNRAS, 396, 1743

Reimer, A., Pohl, M., & Reimer, O. 2006, ApJ, 644, 1118

Reynolds, S. P. 1982, ApJ, 256, 38

Runacres, M. C., & Owocki, S. P. 2002, A&A, 381, 1015

Runacres, M. C., & Owocki, S. P. 2005, A&A, 429, 323

Ryu, D., & Jones, T. W. 1995, ApJ, 442, 228

Ryu, D., Yun, H. S., & Cheo, S.-U. 1995, Journal of Korean Astronomical Society, 28, 223

Ryu, D., Miniati, F., Jones, T. W., & Frank, A. 1998, ApJ, 509, 244

Skilling, J. 1975, MNRAS, 172, 557

van Loo, S., Runacres, M. C., & Blomme, R. 2004, A&A, 418, 717

van Loo, S., Runacres, M. C., & Blomme, R. 2006, A&A, 452, 1011

Wagner, A. Y., Falle, S. A. E. G., Hartquist, T. W., & Pittard, J. M. 2006, A&A, 452, 763

Wright, A. E., & Barlow, M. J. 1975, MNRAS, 170, 41

White, R. L. 1985, ApJ, 289, 698

Appendix A

Energy Losses in CGMV

While Jones & Kang (2005) briefly discusses how to add terms such as energy losses to the DC equation they do not directly show how it is to be done. We will show here how to add in synchrotron and inverse Compton (IC) energy losses to the DC equation in CGMV. These two loss mechanisms are very important when modeling electron acceleration and diffusion, and is commonly desired for most astrophysical situations.

Looking back at eq. (2.1) one can see that additional terms to the DC equation can be added via the S term. For synchrotron energy losses, IC has a similar form, Blandford & Eichler (1987) gives,

$$S = \frac{1}{p^2}\frac{\partial}{\partial p}\left(\frac{p^4 f}{\tau_s}\right) \tag{A.1}$$

Where τ_s is the scaling for the losses which may be dependent on other factors, such as magnetic field energy density, but has the momentum dependence extracted. Eq. (A.1) needs to be transformed such that it will work as a source term for the transformed DC equations for n and g, as seen in eqns (9) and (13) in Jones & Kang (2005). To get the contribution to the n DC eq. one needs to multiply eq. (A.1) by p^2 and integrate over the momentum bin, similar to eq. (2.4).

$$\begin{aligned} S_{n_j} &= \frac{1}{\tau_s}\int_{p_j}^{p_{j+1}} \frac{\partial}{\partial p}(p^4 f)dp \\ &= \frac{1}{\tau_s} p^4 f|_{p_j}^{p_{j+1}} \\ &= \frac{1}{\tau_s}\left(\frac{q_{j+1}-3}{\left(1-d_{j+1}^{3-q_{j+1}}\right)} n_{j+1}p_{j+1} - \frac{q_j-3}{\left(1-d_j^{3-q_j}\right)} n_j p_j\right) \end{aligned} \tag{A.2}$$

Where $n_j = \frac{p_j^3 f_j}{q_j-3}(1-d_j^{3-q_j})$ with q_j being the bin slope and $d_j = p_{j+1}/p_j$.
The source term for g is achieved by multiplying eq. (A.1) by p^3 and integrating.

$$\begin{aligned} S_{g_j} &= \frac{1}{\tau_s}\int_{p_j}^{p_{j+1}} p\frac{\partial}{\partial p}(p^4 f)dp \\ &= \frac{1}{\tau_s}\left(p^5 f|_{p_j}^{p_{j+1}} - \int_{p_j}^{p_{j+1}} p^4 f dp\right) \\ &= \frac{1}{\tau_s}\left(\frac{q_{j+1}-4}{\left(1-d_{j+1}^{4-q_{j+1}}\right)} g_{j+1}p_{j+1} - \frac{q_j-4}{\left(1-d_j^{4-q_j}\right)} g_j p_j - \frac{(q_j-4)}{(q_j-5)}\frac{(1-d_{j+1}^{5-q_{j+1}})}{(1-d_{j+1}^{4-q_{j+1}})} g_j p_j\right) \end{aligned} \tag{A.3}$$

Where $g_j = \frac{p_j^4 f_j}{q_j-4}(1-d_j^{4-q_j})$. One can now see by analogy how one would go about adding terms to the DC eq. in the CGMV formulation. One simply takes the term and multiplies by either p^2 or p^3 depending on whether one is treating n or g then integrate the expression across a bin.

Appendix B

2-D Cylindrical Coordinates in CGMV

Other geometries than Cartesian have been used in the past to exploit symmetries in the system being modeled (e.g. Kang & Jones (2006)). For several astrophysical situations, such as supernovae and stellar winds, cylindrical coordinates are an appropriate coordinate system. For this exercise we will treat 2-D cylindrical coordinates with the z-axis being the symmetry axis. In order to see what modifications we need to make in cylindrical coordinates let us consider the multidimensional form of the DC eq.

$$\frac{df}{dt} = \frac{1}{3}(\nabla \cdot \vec{u})\frac{\partial f}{\partial y} + \nabla \cdot (\overleftrightarrow{\kappa} \cdot \nabla f) \tag{B.1}$$

We have dropped the source terms in this equation as we wish to focus on the diffusion and momentum convection components of the equation. We will assume that the diffusion coefficient, $\overleftrightarrow{\kappa}$, does not have any off diagonal terms for this exercise. In cylindrical coordinates the z coordinate looks exactly the same as Cartesian but the r coordinate looks like

$$\frac{df}{dt} = \frac{1}{3r}\frac{\partial (r u_r)}{\partial r}\frac{\partial f}{\partial y} + \frac{1}{r}\frac{\partial}{\partial r}\left(r \kappa_r \frac{\partial f}{\partial r}\right) \tag{B.2}$$

The first term is solved in CGMV, for which the only correction is the treatment of the divergence of the velocity in the radial direction. The second term is solved using the

CN scheme which is a bit more complicated. We will compute the case for f here with the extension to n and g being analogous. For the CN scheme we solve the following equations:

$$\begin{aligned}
\frac{\partial f}{\partial t} &= \frac{1}{r}\frac{\partial}{\partial r}\left(r\kappa_r\frac{\partial f}{\partial r}\right) = \frac{1}{r}\frac{\partial(rF)}{\partial r} \\
f_i^{k+1} &= f_i^k - \frac{1}{r_i}\frac{\Delta t}{\Delta x}\left(r_{i+1/2}\bar{F}_{i+1/2} - r_{i-1/2}\bar{F}_{i-1/2}\right) \\
\bar{F}_{i+1/2} &= -\kappa_{i+1/2}\left(\frac{\bar{f}_{i+1} - \bar{f}_i}{\Delta x}\right) \\
\bar{f}_i &= \frac{1}{2}\left(f_i^{k+1} + f_i^k\right) \\
\kappa_{i+1/2} &= \frac{1}{2}\left(\kappa_{i+1} + \kappa_i\right)
\end{aligned} \tag{B.3}$$

Where k is the time step counter and i is the position in r. After some algebra one can produce the following equations

$$\begin{aligned}
A_i^+ f_{i+1}^{k+1} + A_i^0 f_i^{k+1} + A_i^- f_{i-1}^{k+1} &= C_i^0, \\
a_{i+1/2} = r_{i+1/2}\kappa_{i+1/2}, \qquad b_i = \frac{1}{r_i}\delta, \qquad \delta &= \frac{\Delta t}{2(\Delta x)^2} \\
A_i^+ &= -b_i a_{i+1/2} \\
A_i^0 &= 1 + b_i(a_{i+1/2} + a_{i-1/2}) \\
A_i^- &= -b_i a_{i-1/2} \\
C_i^0 &= b_i a_{i+1/2} f_{i+1}^k + (1 - b_i(a_{i+1/2} + a_{i-1/2}))f_i^k + b_i a_{i-1/2} f_{i-1}^k
\end{aligned} \tag{B.4}$$

As can be seen the actual changes that need to be made to the CN scheme can be applied as a correction to κ and δ. Precautions should be taken when the radius is small or zero. Also the radius should be always positive.